RESEARCH ARTICLE SUMMARY

CELL BIOLOGY

Epithelial tension controls intestinal cell extrusion

Daniel Krueger*†, Willem Kasper Spoelstra†, Dirk Jan Mastebroek, Rutger N. U. Kok, Shanie Wu, Mike Nikolaev, Marie Bannier-Hélaouët, Nikolche Gjorevski, Matthias Lutolf, Johan van Es, Jeroen van Zon*, Sander J. Tans*, Hans Clevers*

Full article and list of author affiliations: https://doi.org/10.1126/science.adr8753

INTRODUCTION: The intestinal epithelium is a protective barrier between the body and the luminal gut content. Disruption of this barrier is a hallmark of diseases such as inflammatory bowel disease and tufting enteropathy. To preserve tissue homeostasis, the epithelium undergoes self-renewal, during which new cells are born continuously and older cells are removed through extrusion. A commonly proposed model suggests that proliferation-induced crowding triggers extrusion at the villus tip. This model, although conceptually attractive, remains untested owing to the challenges of studying mechanical forces and cellular dynamics within the intestine's complex architecture. Identifying cues that govern extrusion is essential for understanding how the intestine maintains homeostasis and how extrusion fails in disease.

RATIONALE: We hypothesized that intestinal cell extrusion is regulated by intercellular force transmission arising from crowding or other mechanical interactions. To test this, we used intestinal organoids that recapitulate key features of the native tissue while enabling real-time manipulation and observation from multicellular to subcellular levels. Our strategy combined long-term live imaging with automated cell tracking such that we could follow extrusion events in space and time. To mimic in vivo tissue topology, organoids were cultured on three-dimensionally shaped hydrogels. CRISPR-engineered fluorescent tagging and optogenetic control of myosin II enabled both visualization and induction of contractility, and laser ablation provided acute mechanical perturbations. Key findings were validated in mouse intestinal tissue. This multiscale approach allowed us to dissect the spatiotemporal force dynamics that govern extrusion.

RESULTS: We found that cells extrude from regions of the intestinal villus that are under tension. This tension is generated by a dynamically contracting actomyosin network at the cell base and reveals the "tug-of-war" behavior of cells. Optogenetic activation of contractility and mosaic organoids consisting of cells with different levels of contractility showed that highly contractile cells can drive extrusion of less-contractile neighbors. Reducing a cell's contractility genetically or disrupting its basal cortex by laser ablation also prompted extrusion, showing that the abrupt loss of the ability to generate tension triggers cell extrusion. Extrusion involved myosin II up-regulation in the extruding cell and its neighbors, reflecting a coordination at the tissue level. Lastly, in a model of congenital tufting enteropathy—caused by epithelial cell adhesion molecule (Epcam) loss and associated with hyperactive myosin II—we observed excessive contractility, which disrupted tissue architecture, increased extrusion rates, and in mosaics led to the myosin-dependent preferential elimination of less-contractile wild-type cells.

CONCLUSION: Our results support a tension-based model for the regulation of cell extrusion in the intestine. A dynamic and contractile actomyosin network generates tissue-scale tension, and cells that fail to produce sufficient force to counteract pulling by their neighbors are preferentially removed. This tug-of-war mechanism maintains mechanical integrity by eliminating the tissue's weakest links. Our findings reframe intestinal homeostasis as an active, force-regulated process. They also show how differences in contractility, such as those observed in congenital tufting enteropathy, can lead to abnormal extrusion and disrupted epithelial structure. These insights suggest that targeting force-generating pathways may provide potential therapeutic strategies for diseases in which epithelial barrier function is compromised. ☐

---

*Corresponding author. Email: h.clevers@hubrecht.eu (H.C.); s.tans@amolf.nl; (S.J.T.); j.v.zon@amolf.nl (J.V.Z.); d.krueger@hubrecht.eu (D.K.) †These authors contributed equally to this work. **Cite this article as D. Krueger *et al.*, *Science* 389**, eadr8753 (2025). DOI:10.1126/science.adr8753

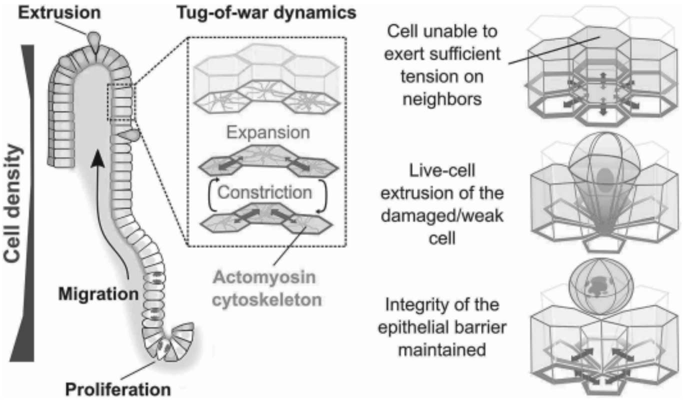

Tug-of-war–like competition between intestinal epithelial cells regulates cell extrusion. Cells in the intestinal epithelium proliferate in the crypt, migrate up the villus, and typically extrude near the villus tip. In the villus, cells exert highly dynamic tension forces on their neighbors. Mechanically compromised cells that cannot exert sufficient tension extrude in order to maintain the integrity of the intestinal epithelial barrier.

CELL BIOLOGY

Epithelial tension controls intestinal cell extrusion

Daniel Krueger[1,2]*†, Willem Kasper Spoelstra[3]†, Dirk Jan Mastebroek[1], Rutger N. U. Kok[3,4]‡, Shanie Wu[1], Mike Nikolaev[4]§, Marie Bannier-Hélaouët[1,2]§, Nikolche Gjorevski[4]§, Matthias Lutolf[4]§, Johan van Es[1,2], Jeroen van Zon[3]*, Sander J. Tans[3,5]*, Hans Clevers[1,2]*¶

Cell extrusion is essential for homeostatic self-renewal of the intestinal epithelium. Extrusion is thought to be triggered by crowding-induced compression of cells at the intestinal villus tip. In this study, we found instead that a local "tug-of-war" competition between contractile cells regulated extrusion in the intestinal epithelium. We combined quantitative live microscopy, optogenetic induction of tissue tension, genetic perturbation of myosin II activity, and local disruption of the basal cortex in mouse intestines and intestinal organoids. These approaches revealed that a dynamic actomyosin network generates tension throughout the intestinal villi, including the villus tip region. Mechanically weak cells unable to maintain this tension underwent extrusion. Thus, epithelial barrier integrity depends on intercellular mechanics.

The intestinal epithelium is a defensive barrier protecting the underlying tissue from microbiota, pathogens, and acidity. The turnover of cells within the intestinal epithelium is rapid, and most cells are replaced within a few days (*1*, *2*). Stem cells are generated in the crypt and then migrate upwards to the tissue protrusions called villi (*3*) as they differentiate and acquire specialized function (*4*, *5*). After several days, mature cells are extruded in a controlled manner into the gut lumen (*6*–*8*). The mechanisms regulating cell extrusion in the intestine are not well understood (*9*), and current models are largely inferred from nonmammalian model organisms and systems. Apoptotic cell extrusion has been demonstrated to regulate cell numbers in cell lines, *Drosophila* (*10*), and the zebrafish epidermis (*11*, *12*). However, mouse intestines with genetic knockouts of key apoptotic pathway components such as Bcl-2, Bax, Bcl-w, and Caspase-3/7/8 display normal villus morphology, indicating a normal regulation of homeostatic cell extrusion (*13*–*16*). In Madin-Darby canine kidney (MDCK) cell monolayers (*17*), zebrafish epidermis (*17*), and the *Drosophila* notum (*18*, *19*), extrusion is driven by increased cell density. These findings have inspired a model for the mammalian intestinal epithelium, in which the flow of cells to the villus causes cell crowding. In that model, compression forces at the villus tip would trigger extrusion [see (*20*) and (*21*) for recent reviews]. However, cell extrusion is enriched at—but not limited to—the villus tip: The frequency of cell extrusion gradually increases along the villus shaft and peaks at the villus tip (*22*, *23*). Yet cell density is high in the crypt and at the villus base, lower along the villus shaft, and returns to villus-base levels at the villus tip (*3*). Thus, crowding alone seems insufficient to explain the extrusion pattern.

Previous work suggests that active cell migration along the villus leads to cell crowding at the villus tip, while leaving the villus bottom under tension, as indicated by laser ablation experiments (*3*). Cell contractility and mechanical forces have been implicated in the regulation of cell extrusion or delamination in other epithelial systems. For example, induction of Ras homolog (Rho) kinase—an upstream regulator of myosin II—reduces extrusion in the *Drosophila* notum and zebrafish epidermis (*24*–*26*). In the *Drosophila* abdominal epidermis, extrusion is associated with pulsatile actomyosin contractions, and extrusion frequency increases under conditions of elevated tensile stress (*27*). By contrast, elevated cortical tension inhibits the apical extrusion of oncogenic H-RasV12 cells in liver epithelial monolayers (*28*). Thus, the role of mechanical force is important for cell extrusion and depends on the tissue context but has remained largely unaddressed in the intestinal villi.

Cells extrude from regions under tension in a crowding-independent manner

Mouse intestinal organoids faithfully recapitulate the self-renewal processes of the gut epithelium (*6*). At the tips of organoid buds (the equivalents of the crypts of Lieberkühn), Lgr5$^+$ stem cells are interspersed between Paneth cells, the latter serving as a source of niche signals. Daughter cells rapidly proliferate and move away from the buds toward a central villus domain. As they reach the villus domain, the cells differentiate into one of the mature intestinal epithelial cell types, the most abundant being the enterocyte. To establish an experimental platform for mechanistic studies of the cell extrusion process, we developed a method to quantify the localization of the cell extrusion events. We imaged mouse intestinal organoids expressing a histone 2B (H2B)–mCherry nuclear marker over multiple days. Using a neural network approach (*29*), we tracked single cells and identified hundreds of extruding cells (Fig. 1, A and B, and movie S1). We observed two distinct extrusion modes: One showed fragmented nuclei before extrusion, indicative of extrusion driven by apoptosis; the other showed extrusion with intact nuclei, indicating a live-cell process (Fig. 1, C and D, and fig. S1A). Apoptotic cell extrusion was the predominant form in the stem cell–containing crypt region, where, under physiological in vivo conditions, cell extrusion is typically rare. However, most (92%) of the extrusions in the villus-like region were live-cell extrusions (Fig. 1E and fig. S1B). Next, we tested whether cell extrusion was determined by an intrinsic timer set before the last division (*30*). The lifetime of cells—defined as the period between the last division and extrusion—showed major differences for apoptotic and live-cell extrusion. The median lifetime of apoptotic cells was short (6 hours) and similar between sister cells: Cells had an 82% chance of extruding in an apoptotic manner if their sister also did so (fig. S1C). Thus, apoptotic cell extrusion appears to result from fatal errors in the mother's cell cycle or during mitosis (*31*). The lifetimes of cells undergoing live-cell extrusion were broadly distributed, with a median of 27 hours (Fig. 1F and fig. S1, D and E). The lifetime of one sister cell undergoing live-cell extrusion poorly predicted the lifetime of the second sister (fig. S1F). Conclusively, live-cell extrusion is not controlled by a timer set before the cell's birth.

To test whether tissue crowding triggers live-cell extrusion in the intestinal epithelium, we analyzed the positions of extrusion events and the local cell density by tracking nuclei. Nuclei of neighbors of extruding cells initially moved away from the extruding cell and returned directly after extrusion so that the local cell density recovered to pre-extrusion levels within approximately 45 min (fig. S1, G and H). Furthermore, cell extrusion events were spatially and temporally correlated; cells tended to extrude close to each other and shortly after a nearby cell had extruded, typically when cells from different crypts came into contact (fig. S1, I to L). Notably, extrusions were not

---

[1] Hubrecht Institute, Royal Netherlands Academy of Arts and Sciences (KNAW) and University Medical Centre Utrecht (UMC), Utrecht, Netherlands. [2] Oncode Institute, Hubrecht Institute, Utrecht, Netherlands. [3] AMOLF Institute, Amsterdam, Netherlands. [4] École Polytechnique Fédérale de Lausanne/Institute of Human Biology, Basel, Switzerland. [5] Bionanoscience Department, Kavli Institute of Nanoscience Delft, Delft University of Technology, Delft, Netherlands. ***Corresponding author. Email: h.clevers@hubrecht.eu (H.C.); s.tans@amolf.nl (S.J.T.); j.v.zon@amolf.nl (J.V.Z.); d.krueger@hubrecht.eu (D.K.)** †These authors contributed equally to this work. ‡Present address: Center for Molecular Medicine, UMC Utrecht, Netherlands. §Present address: Institute of Human Biology (IHB) Roche Pharma Research and Early Development, Basel, Switzerland. ¶Present address: Roche Pharma, Research and Early Development (pRED) of F. Hoffmann-La Roche, Basel, Switzerland.

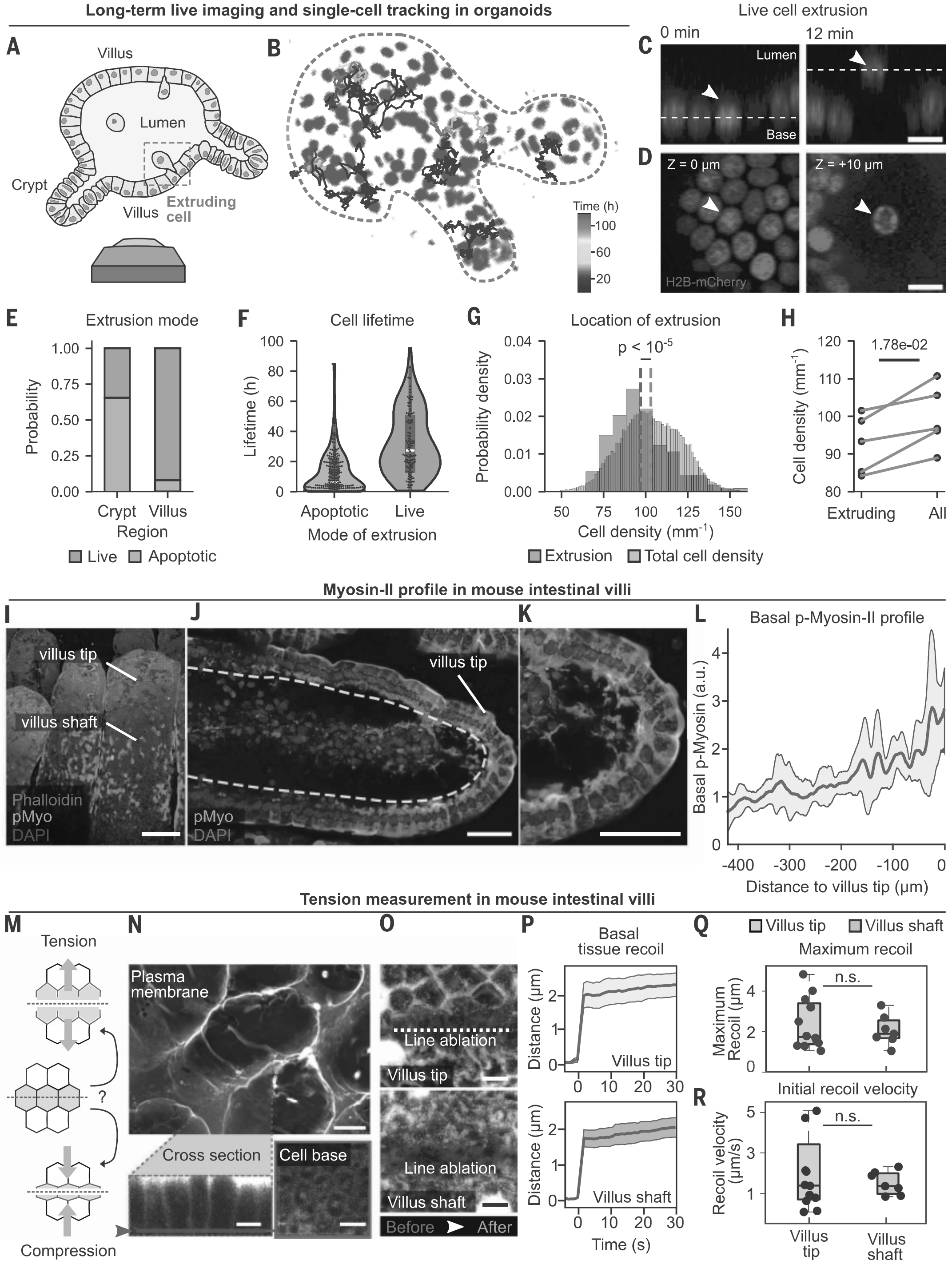

Fig. 1. Intestinal live-cell extrusion occurs predominantly from regions under tension. (**A**) Live imaging and single-cell tracking of nuclear-labeled intestinal organoids. (**B**) Time-colored tracks overlaid on a tracked organoid. (**C** and **D**) Cross section (C) and top view (D) of a live-cell extrusion, defined by the presence of an unfragmented nucleus at its final time point in the epithelium. Arrowheads indicate the extruding cell. Scale bars, 10 μm. (**E**) Proportions of apoptotic and live-cell extrusions in villus and crypt. (**F**) Lifetime distribution of 217 apoptotically and 114 live extruding cells. (**G**) Cell density around 142 extruding cells (green) and nonextruding cells from $n = 5$ organoids (Mann-Whitney U test on individual densities). Cell density was defined as the reciprocal of the average distance to the six nearest neighbors. Binning is for visualization only. (**H**) Average cell density of extruding and nonextruding cells per organoid ($n = 5$ organoids; two-sided corrected Student's t test). (**I** to **K**) Whole-mount stain of mouse intestinal villi. (I) Overview showing F-actin (phalloidin, magenta), active myosin II (pMyo, green), and nuclei [4′,6-diamidino-2-phenylindole (DAPI), blue]. Scale bar, 100 μm. (J) Cross section of an intestinal villus stained for pMyo (green) and nuclei (magenta). Dashed line marks the basal surface. (K) Zoom of villus tip in (J). (**L**) Basal myosin II profile along the villus (mean ± SD; $n = 6$ villi). [(J) and (K)] Scale bar, 25 μm. (**M**) Schematic: Line cut reveals tension by recoil, compression by condensation. (**N**) Dissected mouse intestine stained with membrane marker (CellMask-Orange). (Top) Overview of villi. (Bottom left) Villus cross section with magenta line marking the basal plane (shown in bottom right). Line ablation was performed at this basal section. Scale bars: 50 μm (top), 10 μm (bottom). (**O**) Line ablation (dashed line) at the villus tip (top) and shaft (bottom). Magenta shows the basal surface before ablation; green shows basal surface after ablation. Scale bars, 10 μm. (**P**) Orthogonal recoil after basal line ablation at the villus tip (top) and shaft (bottom). Bold lines indicate mean; shaded areas indicate SEM. (**Q** and **R**) Maximum recoil (Q) and initial velocity (R) after basal ablation at villus tip and shaft (two-sided Student's t test). [(P) to (R)] Data from 12 villus tips, 7 villus shafts ($n = 3$ mice).

concentrated in regions of high cell density. Instead, cells showed a tendency to extrude from areas of average—or low—cell density within the villus-like domain (Fig. 1, G and H). Thus, cell extrusion in intestinal organoids is not primarily driven by tissue crowding.

These findings prompted us to investigate whether alternative mechanisms involving mechanical forces underlie cell extrusion. We examined the actomyosin network along the intestinal villus by staining whole-mount mouse intestines for active (phosphorylated) myosin II, the primary force-generating motor protein. We observed a pronounced accumulation of myosin II at the basal surface of villus cells, which increased from the base to the tip (Fig. 1, I to L, and fig. S2, A to D). This myosin II accumulation suggested the generation of tensile forces, prompting us to question whether compression forces prevail at the villus tip.

To test whether the intestinal epithelium at the villus tip was under tension or compression in vivo, we dissected small intestines from wild-type (WT) mice and immediately afterwards applied line-shaped laser ablations at different regions of the villus: If the tissue were under tension, one would expect an outward retraction orthogonal to the cut line, whereas a compressed tissue would shrink or remain static (Fig. 1M). In one set of experiments, we ablated the basal surface of a lateral group of 6 to 10 adjacent cells using a line cut spanning ~60 μm (fig. S2, E and F)—sizeable enough to integrate the response of multiple cells, yet within the geometric constraints imposed by the villus curvature (*32*). These cuts were performed both at the villus shaft and at the villus tip region. Upon ablation at the basal surface, we observed a rapid outward tissue recoil orthogonal to the ablation line in both regions (Fig. 1, N to P; fig. S2F; and movie S2) with a similar maximum recoil and initial recoil velocity of approximately 1.4 μm/s (Fig. 1, Q and R). In another setup, we ablated entire single cells along their apical-basal axis at the villus tip rather than cutting only their basal surface. Here too, neighboring cells consistently retracted away from the ablated cell (fig. S2, G to J). Thus, the mouse villus tip, the main region of cell extrusion, is under tension rather than compression.

A highly dynamic actomyosin network underlies basal tissue tension

Given the above findings and the known cytoskeletal remodeling required for cell extrusion, we hypothesized that local tensile tissue forces could play a role in its regulation. We generated intestinal organoid reporter lines for myosin II by integrating a fluorescent tag (mNeonGreen) in the endogenous locus of different subunits of the myosin II multiprotein complex (Fig. 2, A and B, and fig. S3, A to D). The reporter targeting myosin regulatory light chain (Myl12a) colocalized strongly with antibodies for active (phosphorylated) myosin II (fig. S3, E and F). It was also enriched at sites of actomyosin contraction, for example at the cytokinetic furrow during cell division (fig. S3G). During cell extrusion, myosin II rapidly increased at the cell base and redistributed in a zipper-like pattern along the lateral surface toward the apex, before the cell was expelled apically into the organoid lumen (Fig. 2C, fig. S3H, and movie S3). This suggests that myosin II–mediated contraction exerts the force necessary to extrude a cell into the lumen.

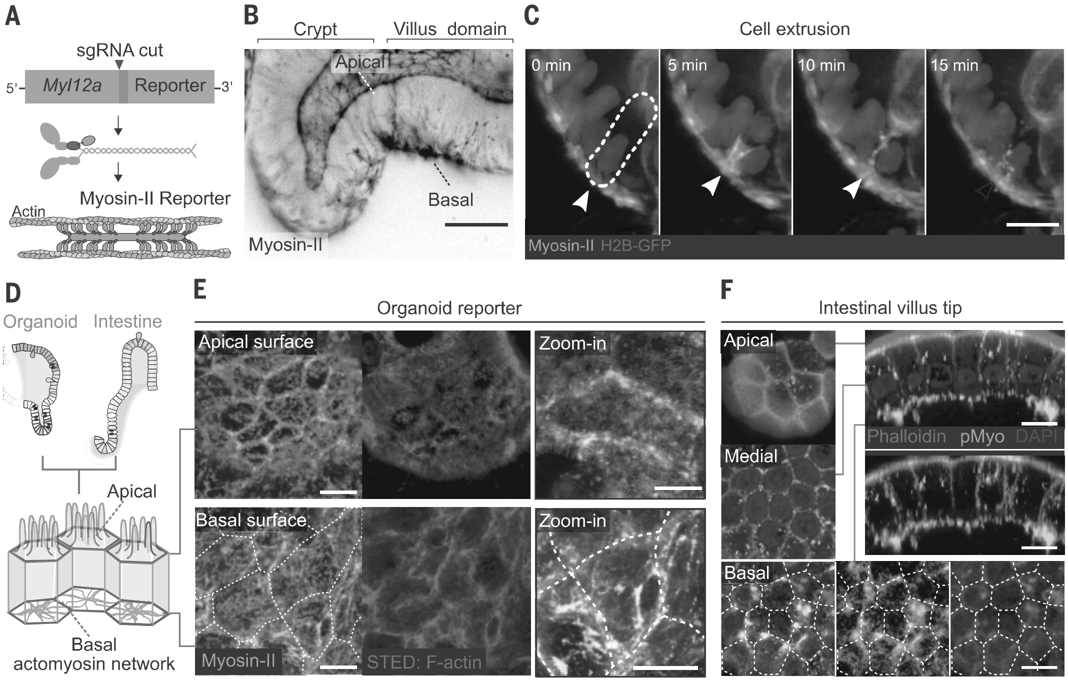

Fig. 2. A basal actomyosin network connects intestinal epithelial cells. (**A**) Generation of fluorescent reporter organoid line for myosin II activity. The endogenous myosin regulatory light chain gene *Myl12a* was tagged with a fluorescent fusion protein (mNeonGreen). (**B**) myosin II–mNeonGreen reporter organoid showing myosin II enrichment at the basal surface in the villus-like domain. (**C**) Time-lapse image of an extruding cell in an organoid coexpressing myosin II–tdTomato (green) and H2B-GFP (blue). Dashed line marks the cell just before extrusion. Scale bar, 20 μm; cell was imaged with light-sheet microscopy. (**D**) Schematic of cells in the villus region of intestinal organoids and in vivo villus tips (light blue). The apical surface facing the lumen features actin-rich microvilli and a cortical cytoskeleton lining the plasma membrane. (**E** and **F**) The basal actomyosin network (green) connects cells through junctions. (E) Super-resolution STED microscopy images of the apical (top row) and basal (bottom row) actomyosin network stained for F-actin (phalloidin, magenta, middle), in an organoid expressing myosin II–mNeonGreen (green, left). The right-hand images show a zoom-in of a single cell with superimposed actin and myosin signals. Scale bars: 10 μm (left), 5 μm (zoom-ins). (F) High-resolution confocal images of cells of the mouse intestinal villus tip with top views of the apical (top), medial (middle), and basal (bottom) section and cross sections of the entire cell (right) stained for F-actin (phalloidin, magenta), phosphorylated myosin (green), and nuclei (DAPI, blue). Scale bars, 5 μm. Dashed lines in (E) and (F) indicate the cell boundaries.

The myosin II intensity profile along the organoid's crypt-villus axis showed a strong apical signal in the crypt region, diminishing toward the villus domain (*33*, *34*) (fig. S3, I and J, and movie S4). Conversely, basal myosin II exhibited its highest intensity in the villus region, both in organoids and in tissue (Fig. 1L and fig. S3, I and J). Stimulated emission depletion (STED) super-resolution microscopy identified two distinct myosin II localization patterns: a junctional pool, which lined the cell boundaries and predominated the apical surface, and a medial pool where myosin II coalesced in the cell center and extended radially to cell-cell junctions, predominantly found at the basal cell surface in the villus domain (Fig. 2, D and E). The overlap of medial and junctional myosin II at the basal surface creates an interconnected actomyosin network, similar to those facilitating coordinated cell movements in other epithelial tissues (*35*, *36*). We confirmed that this organization was also prevalent in vivo throughout the intestinal villi, both in the shaft region and at the villus tip (Fig. 2F and fig. S3K). The prominent basal enrichment of both medial and junctional myosin II suggests a network capable of generating tissue tension through coordinated contractions (*37*, *38*).

To reconstruct the force-transmission between cells in an in vivo-like fashion, we grew myosin II reporter organoids on three-dimensional (3D) hydrogel substrates that closely mimic the tissue architecture of the intestine (Fig. 3A and fig. S3L) (*8*). Live-cell imaging of the synthetic villus tip showed dynamic basal myosin II remodeling, revealing a pulsatile reorganization of the actomyosin network on the basal surface of the intestinal epithelium (Fig. 3, B to F; fig. S4, A to E; and movie S5). With our earlier data, this suggested that although the tissue is permanently under tension, individual cells' contractility dynamically changes. This is reflected in transient myosin II accumulation that was accompanied by a concomitant decrease of basal cell area, presumably due to the myosin II–mediated pulling forces (Fig. 3, C to F, and fig. S4, A to E). Conversely, basal expansion was accompanied by decreasing myosin II levels, and myosin II minima coincided with an increase of basal area (Fig. 3, C to F, and fig. S4, A to E). Pulsatile actomyosin networks have been described in other epithelia to coordinate cellular rearrangements such as the inward folding of a tissue (*37*, *38*) or delamination of individual cells (*39*). These dynamics allow cells to continuously interact with their neighbors, probe the environment, and enable tissue-level coordination (*38*, *40*). Such tissue-level coordination was evident in the inverse relationship between the cell areas of neighboring cells: When a central cell constricted, its neighbors expanded (fig. S4, F and H). Thus, cells in the villus region dynamically regulate myosin II, driving pulsatile basal area changes. Through mechanical coupling via cell junctions, myosin II–generated forces appear to propagate to adjacent cells, orchestrating a tissue-wide "tug-of-war."

Cell extrusion is regulated by a cell's ability to exert tissue tension

To determine whether tissue tension generated by basal actomyosin contractions has a role in regulating cell extrusion, we established an optogenetic method to control myosin II–mediated contractility, and thereby tissue tension, in intestinal organoids. We integrated a doxycycline-inducible optogenetic system called opto-Arhgef11 (*41*) into intestinal organoids. Opto-Arhgef11 is based on the light-dependent heterodimerization of the photosensor cryptochrome 2

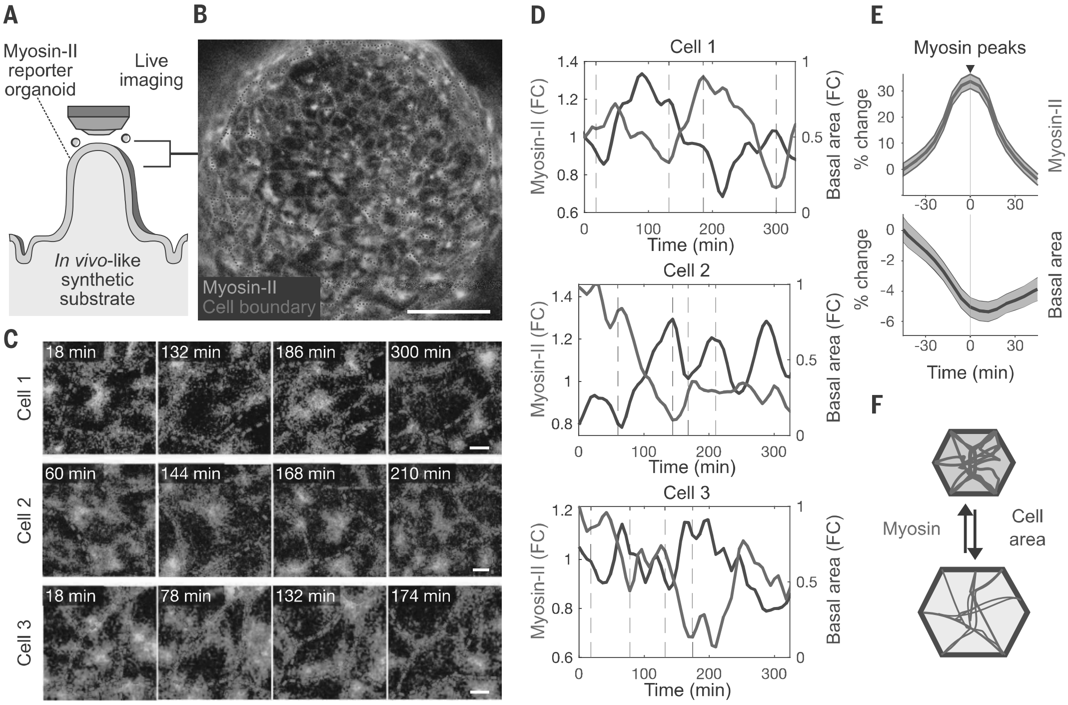

Fig. 3. Intestinal epithelial cells use their basal cytoskeleton to exert highly dynamic pulling forces on their neighbors. (**A**) Experimental setup to analyze basal cell dynamics at the villus domain using crypt-villus substrates mimicking the in vivo tissue architecture. (**B** and **C**) The myosin reporter line coexpressing a membrane-bound mCherry fluorescent marker was grown on crypt-villus substrates, and the tip region was imaged using confocal microscopy. Segmented membranes (magenta) were overlayed with the myosin signal (green). (B) Synthetic villus tip. Scale bar, 50 μm. (C) Time-lapse micrographs showing the accumulation and dissipation of myosin II in cells causing basal cell–area pulsations. Scale bar, 5 μm. (**D**) Mean myosin II signal (green, left axis) and corresponding basal cell area (magenta, right axis) of three cells indicated in panel (C). Gray vertical lines indicate the respective time points of the micrographs in (C). (**E**) Time-aligned mean traces of myosin II peaks (top) reveal a concurrent decrease in basal cell area (bottom). Solid lines indicate mean fold change (FC); shaded areas indicate SEM. (**F**) Schematic illustrating the observed anticorrelation between basal myosin II and basal area.

(CRY2), fused to Rho guanine nucleotide exchange factor 11 (Arhgef11) and its interaction partner cryptochrome-interacting basic-helix-loop-helix (CIBN), which is anchored at the plasma membrane (Fig. 4A). Arhgef11-CRY2 remained cytoplasmic and inactive in the dark but rapidly translocated to the plasma membrane upon blue-light excitation (Fig. 4B). On the membrane, it initiated the endogenous Rho signaling cascade, which triggers myosin II–induced cell contractility and increases tissue tension. Indeed, local photoactivation caused a focused contraction of the organoid, which relaxed again owing to the dissociation of CRY2-CIBN in the absence of blue light (Fig. 4C and movie S6). Staining uniformly photoactivated opto-Arhgef11 organoids for phosphorylated myosin II revealed a ~1.7-fold overall increase in active myosin II levels, with minimal impact on its subcellular distribution (fig. S5, A to C).

To test the impact of myosin II activity on cell extrusion systematically, we grew opto-Arhgef11 organoid cells on synthetic 3D hydrogel substrates and measured the rate of extrusion at the villus tip (Fig. 4D and fig. S5D). Continuous global photoactivation led to increased

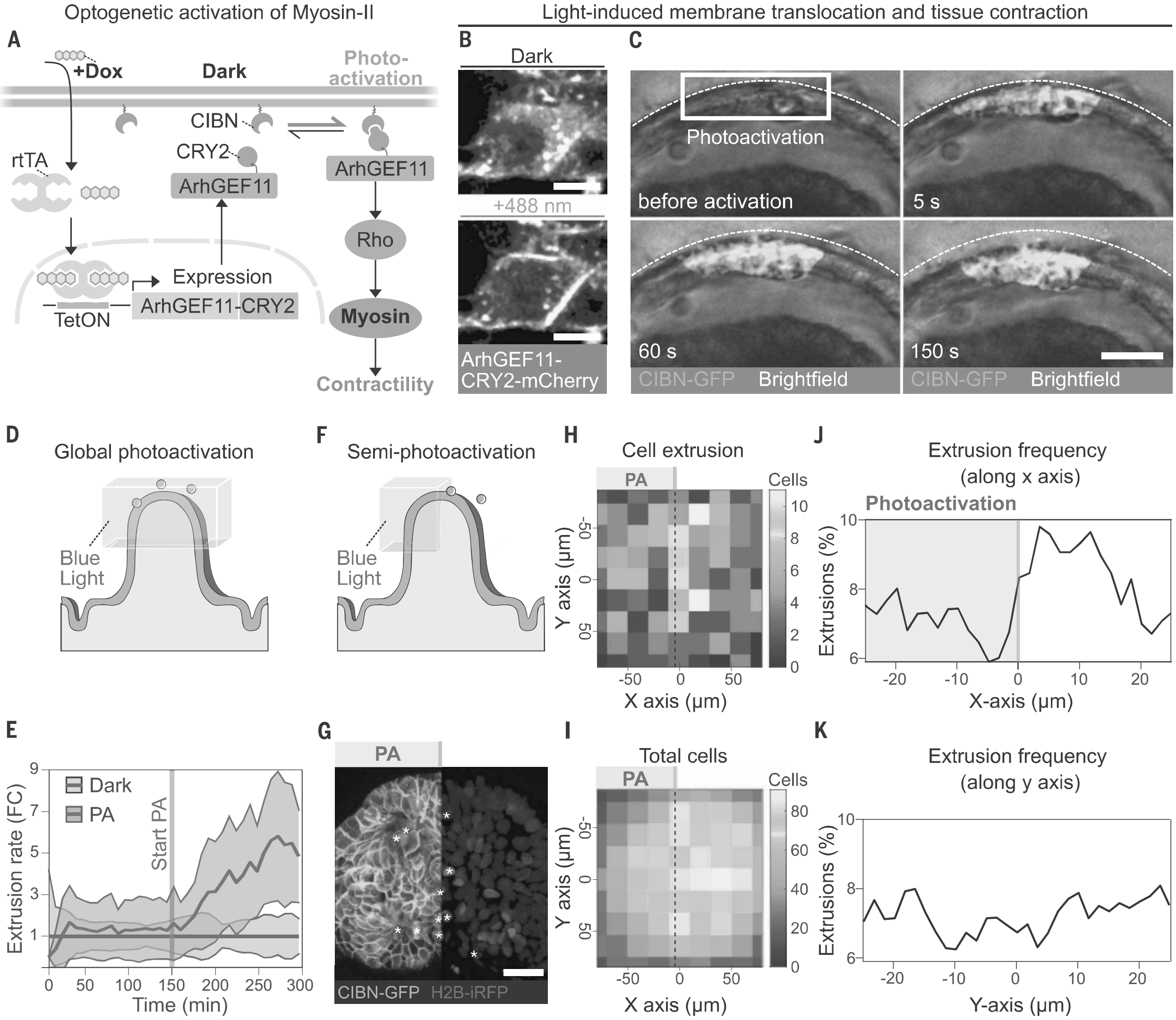

Fig. 4. Differences in intercellular tension influence cell extrusion at the villus tip. (**A**) Schematic of the Arhgef11-CRY2 optogenetic system. Doxycycline (Dox) induces Arhgef11-CRY2 expression through reverse tetracycline-controlled transactivator (rtTA) (TetON). Blue light triggers its dimerization with membrane-bound CIBN, causing Arhgef11 translocation to the membrane, activation of Rho signaling, and increased myosin-driven contractility. (**B**) Arhgef11-CRY2-mCherry was recruited to the membrane upon photoactivation with 488-nm light. Scale bar, 10 μm. (**C**) A group of cells in an opto-Arhgef11 organoid was photoactivated with 488-nm light, inducing contraction. Membrane-anchored CIBN-GFP visible in the photoactivated region (blue). Scale bar, 50 μm. (**D**) Setup to assess acute, global myosin activation: opto-Arhgef11 organoids on crypt-villus substrates were photoactivated at the tip (488 nm). Extrusion was tracked through H2B-iRFP. (**E**) Cell extrusion rates over time in nonphotoactivated (gray) and photoactivated (blue) synthetic villi. Villi were imaged with 640-nm light before 488-nm photoactivation (PA) (vertical line), which triggered up to a fivefold increase in the average extrusion rate. Rates are shown as fold change (FC) relative to dark control (mean ± SD; 19 dark, 13 photoactivated villi). (**F** to **K**) Patterned activation of myosin-mediated tension: One half of synthetic villus tips were photoactivated (blue) to create an artificial boundary between myosin-activated and nonactivated cells ($n = 24$ villi). (F) Schematic illustrating the setup. (G) Confocal image of a villus tip with cells coexpressing opto-Arhgef11 (CIBN-GFP, cyan) and H2B-iRFP (magenta). Asterisks mark extrusion events detected within 45 min. [(H) and (I)] Heatmaps showing the location of extrusion events detected within 2.5 hours in 24 villi (H) and total cell density (I). The dashed lines indicate the boundary of the photoactivated region (left). [(J) and (K)] Density of extrusion events averaged along the *x* axis—with photoactivation creating a boundary between photoactivated (left, $x < 0$) and nonactivated (right, $x > 0$) regions (J)—and along the *y* dimension (K). Cells near the pattern boundary extruded less in the photoactivated region and more in the adjacent nonactivated region.

tissue tension compared with nonactivated villi (fig. S5, D to F) and resulted in a fivefold increase in the average extrusion rate (Fig. 4E and fig. S5, G to J). The increase of extrusion rates upon photoactivation was dependent on the addition of doxycycline, confirming that it was not caused by phototoxicity (fig. S5G). The extrusion rate increased readily upon photoactivation, directly after the overall increase of tissue tension. This suggested a link between the tension exerted by cells on their neighbors and extrusion. To test the effect of contractility differences between neighboring cells, we photoactivated one half of the optogenetic villus tip, creating an artificial boundary between myosin-induced and noninduced cells (Fig. 4, F and G). Cell extrusion was increased locally along the boundary of photoactivation (Fig. 4, H to K). Cells most frequently extruded in the nonactivated area facing the boundary with the photoactivated area, whereas cells adjacent to the boundary in the photoactivated region extruded less frequently in comparison (Fig. 4J). Extrusion events were evenly distributed along the photoactivation boundary, indicating that the effect was specific to the illumination pattern (Fig. 4K). Thus, individual cells with lower contractile capabilities compared with the surrounding tissue appear to be more prone to extrusion.

To test this hypothesis, we generated mosaic organoids containing varying ratios of WT cells [tagged with H2B-iRFP (iRFP, infrared fluorescent protein) or H2B-mCherry nuclear markers] and opto-Arhgef11 organoid cells (Fig. 5A). Upon photoactivation, WT cells were significantly overrepresented among extruded cells, particularly in mosaics where WT cells were present as a minority. To quantify this effect, we compared the fraction of WT cells in the extruded population with their overall presence in the organoid, referred to as extrusion enrichment. In organoids where WT cells represented the majority, their extrusion occurred approximately at a rate proportional to their abundance (Fig. 5B). However, as the proportion of opto-Arhgef11 cells increased, WT cells were extruded at a disproportionately higher rate, resulting in a fourfold extrusion enrichment (Fig. 5B). This imbalance was not observed in control organoids that were not induced with doxycycline or not exposed to blue light; in these cases, WT cell extrusion rates remained proportional to their overall presence in the organoid (Fig. 5C). When examining mosaic organoids with a WT cell majority (>50%), the probability of WT-cell extrusion increased with their local proximity to opto-Arhgef11 cells (Fig. 5D). Thus, when optogenetic cells form the majority, the increased tissue-level tension enhances mechanical competition and drives the preferential extrusion of less-contractile WT cells. This effect is further reinforced at the local level because WT cells are more likely to extrude when close to highly contractile optogenetic cells.

To further substantiate these findings, we created a Myh9 heterozygous knockout (*Myh9*$^{+/-}$) organoid line, which has genetically impaired myosin heavy chain function (*33*, *42–45*) (Fig. 5E and fig. S5, K and L). When *Myh9*$^{+/-}$ were combined with WT cells in 3D mosaic organoids, WT cells were consistently underrepresented among extruded cells, whereas *Myh9*$^{+/-}$ cells were overrepresented (Fig. 5, F to I). The observation that *Myh9*$^{+/-}$ extrusion enrichment progressively increased with higher WT cell content argued that higher organoid-level tension promotes the preferential removal of less-contractile cells (Fig. 5I). Indeed, when two *Myh9*$^{+/-}$ populations labeled with different nuclear markers [H2B-mCherry and H2B-GFP (GFP, green fluorescent protein)] were combined, thus eliminating contractility differences, no extrusion bias was observed (Fig. 5, J and K). Thus, cells appear to assess their neighbors' ability to generate tension continuously, resembling a tug-of-war competition for extrusion of weaker cells.

Disruption of the basal cortex integrity causes cell extrusion

To test this tug-of-war hypothesis at the cellular level, we used infrared (IR) laser microsurgery (*33*, *46*) to destabilize the basal cell cortex of individual cells in the villus region (Fig. 6, A and B). Disrupting the basal cytoskeleton consistently led to the extrusion of the targeted cell within 1 hour (Fig. 6, C to G, and movie S7), whereas applying the same laser stimulus directly to the nucleus had no such effect (Fig. 6, E to G, and movie S8). In line with our finding that villus cells are under tension, basally targeted cells expanded within 15 s of ablation, indicating a rapid release of basal tension, whereas expansion was absent when ablation was instead targeted to the nucleus (Fig. 6, H and I). The magnitude of the basal area expansion correlated with the probability of subsequent cell extrusion (Fig. 6J) but not with the extrusion time (Fig. 6K). The reliable induction of cell extrusion after basal expansion further supported the notion that a critical loss of tension-generating capacity due to cytoskeleton disruption is necessary to trigger extrusion.

Directly after basal microsurgery, basal myosin II levels increased at the lateral cell boundaries accompanied by a contraction of the basal surface that brought together the membranes of neighboring cells (Fig. 6, L and M). When myosin II activity was inhibited pharmacologically with blebbistatin, the probability that cells extruded at all within 1 hour decreased from 91% in control organoids to 50% in blebbistatin-treated organoids (Fig. 6N), whereas the duration of the extrusion process after basal microsurgery increased ~twofold (Fig. 6, O and P). Thus, myosin II activity is required for executing cell extrusion and for the timely removal of mechanically weakened cells.

Next, we examined the cellular response when applying the laser stimulus to tension-bearing bi- or tricellular basolateral junctions (Fig. 6Q). This procedure reliably induced the simultaneous extrusion of a duplet or triplet of cells, respectively, showing that the mechanical destabilization of multicellular junctions led to the simultaneous extrusion of the affected cells (Fig. 6R; fig. S6, A to F; and movie S9). Again, when we inhibited myosin II activity with blebbistatin and destabilized the bases through microsurgery, only 50% of the cells extruded within 1 hour, compared with 91% without inhibition (fig. S6, G to I). The stimulated multicell extrusion was driven by the contraction of a common actomyosin accumulation that enclosed all extruding cells (fig. S6J). E-cadherin junctions in neighboring cells were maintained (fig. S6K), and the overall extrusion rate at the organoid level did not significantly increase (fig. S7, A to C), indicating that the epithelial barrier and tissue integrity was maintained. Thus, the epithelium appears to eliminate groups of neighboring cells when they become mechanically compromised and lose the ability to maintain junctional tension.

This prompted us to investigate whether extrusion is driven by cell-autonomous contraction or the coordinated contraction of adjacent cells. We generated mosaic organoids composed of myosin II reporter cells and cells expressing only a nuclear marker and analyzed reporter cells surrounded by nonlabeled neighbors (Fig. 6S), as well as nonlabeled cells surrounded by reporter neighbors (Fig. 6T). Myosin II levels increased markedly in spontaneously (nonablated) extruding cells but also in the cell neighbors (Fig. 6U and movie S10). Thus, the extruding cell appears to trigger an endogenous response to drive its own extrusion through myosin II up-regulation supported by the coordinated myosin II up-regulation in adjacent cells. Together these processes reflect a coordinated tissue behavior to achieve proper contraction, extrusion, and maintenance of epithelial integrity. Thus, intestinal cell extrusion is a coordinated tissue behavior.

Epcam loss distorts tissue tension and epithelial homeostasis in tufting enteropathy

Dysregulation of contractility-based tissue coordination can profoundly impact tissue homeostasis. For example, congenital tufting enteropathy (CTE) is a rare genetic disorder characterized by severe, intractable diarrhea in infants, often leading to intestinal failure. It is caused by mutations in the *epithelial cell adhesion molecule* (*Epcam*) gene (*47*, *48*), which encodes a negative regulator of myosin II: Its loss leads to myosin II hyperactivation (*49*, *50*). The disease phenotype

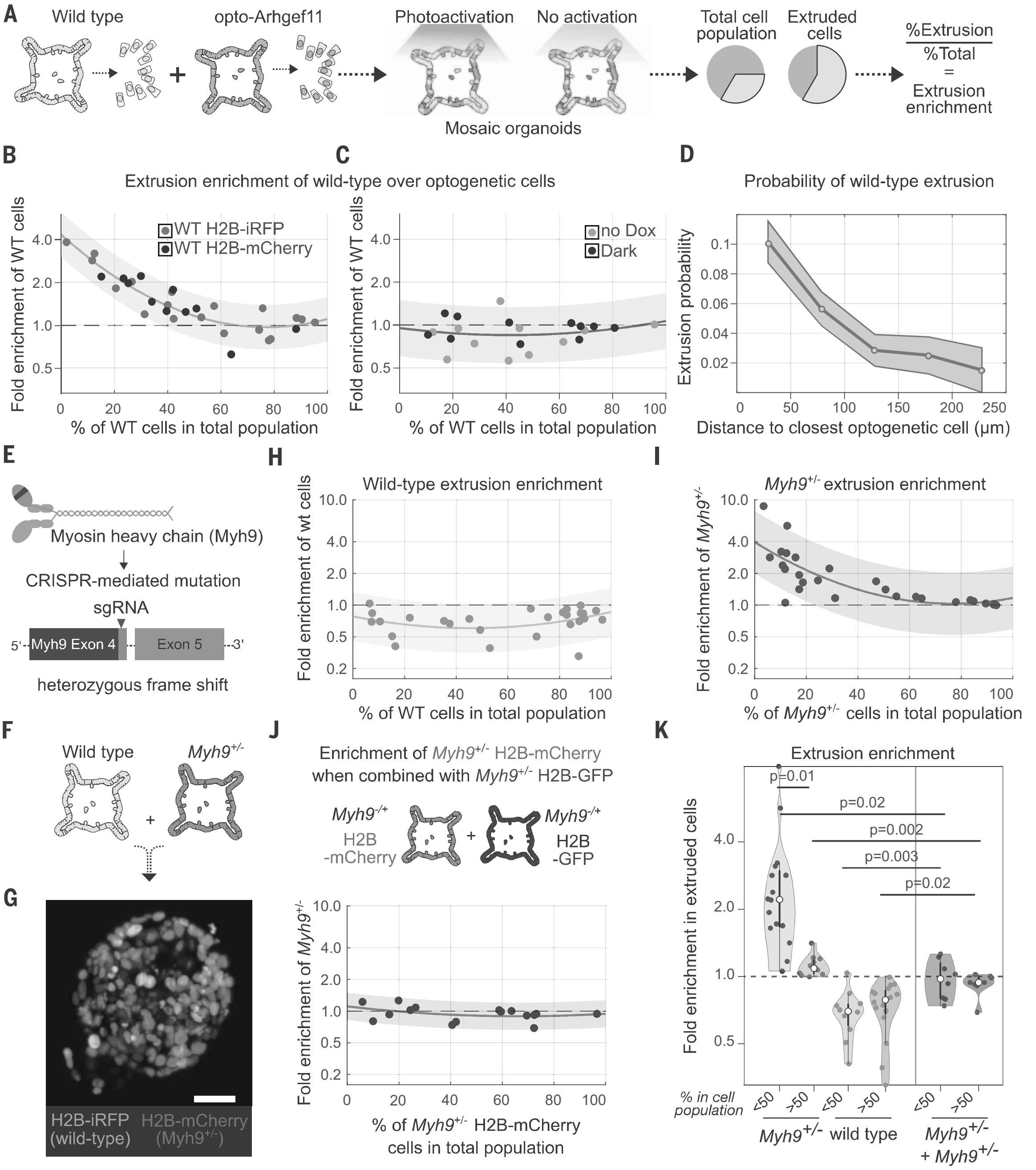

Fig. 5. Contractility differences drive competitive extrusion of myosin II–compromised cells in mosaic organoids. (**A**) Schematic of the setup: wild-type (WT) (green) and opto-Arhgef11 (purple) cells were mixed in mosaic organoids. Photoactivation increased contractility of optogenetic cells. Extrusion enrichment was defined as the ratio of a cell type's fraction in extruded cells to its fraction in the organoid. (**B** and **C**) WT extrusion enrichment in mosaic organoids with varying WT fractions. Each dot: one organoid; solid line: exponential fit with 95% confidence interval (CI) (shaded). The *y* axis shows the log scale. Sample sizes: 31 organoids (B); 22 organoids (C) . (B) WT cells tagged with H2B-iRFP (light blue) or H2B-mCherry (dark blue) showed increased extrusion enrichment when in the minority. (C) Control conditions without doxycycline induction (no Dox) or without photoactivation (Dark) show no significant extrusion enrichment. (**D**) WT cell extrusion probability increases near opto-Arhgef11 cells. Solid line indicates mean; shaded area indicates SEM (82 extrusions from *n* = 6 organoids). (**E**) CRISPR-Cas9 strategy to generate a heterozygous loss-of-function mutant organoid line for Myh9, encoding nonmuscle myosin heavy chain IIA. (**F**) *Myh9*$^{+/-}$ cells (H2B-mCherry) and WT cells (H2B-iRFP) were mixed as single cells to form mosaic organoids. (**G**) Light-sheet image of a mosaic organoid showing WT (green) and *Myh9*$^{+/-}$ (magenta) nuclei. Scale bar, 50 μm. (**H** and **I**) Extrusion enrichment of WT (H) and *Myh9*$^{+/-}$ (I) cells. WT cells are underrepresented, whereas *Myh9*$^{+/-}$ cells are enriched among extruded cells, especially when in the minority (27 organoids). The *y* axes show the log scale. (**J**) Control mosaic organoids with two differentially labeled *Myh9*$^{+/-}$ populations (H2B-mCherry and H2B-GFP) show no extrusion bias (16 organoids). (**K**) Violin plot summarizing fold enrichment of *Myh9*$^{+/-}$ and WT cells in extruded populations, grouped by whether the genotype was in the minority (<50%) or majority (>50%) in the mosaic organoid. Each dot indicates one organoid. *P* values were obtained by two-sided corrected Student's *t* test. The dashed line indicates equal extrusion probability.

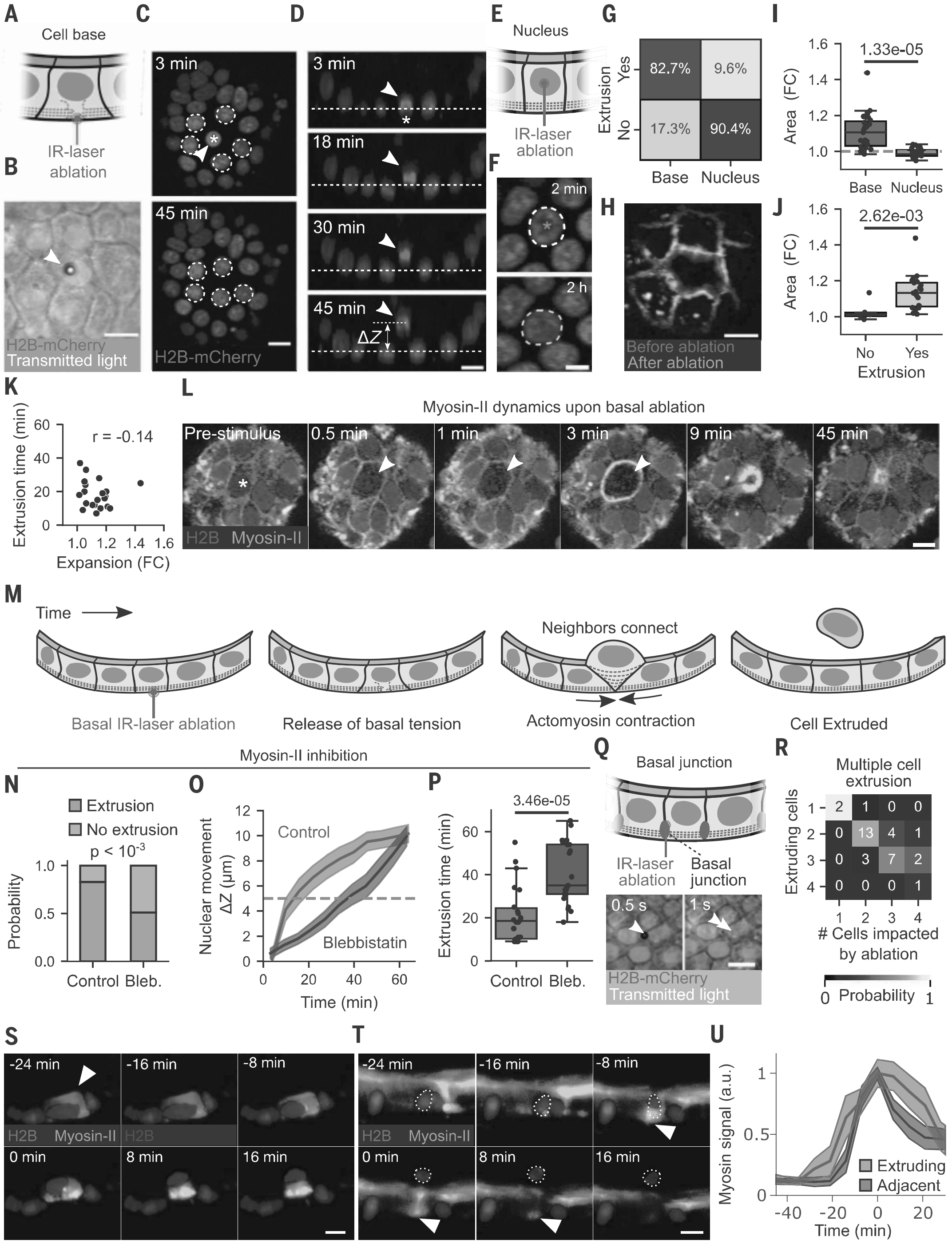

Fig. 6. Release of tissue tension triggers cell extrusion. (**A** to **D**) Point ablation of a single cell's basal surface. (A) Schematic of the point ablation experiment. (B) Brightfield with H2B-mCherry (magenta); [(C) and (D)] Confocal top view (C) and cross section (D) after basal ablation. The arrowheads indicate targeted cells; dashed circles indicate neighbors. "ΔZ" indicates vertical shift of the extruding cell relative to neighbor Z-levels. Scale bars, 10 μm. (**E** and **F**) Schematic (E) and confocal images (F) of point ablation in the nucleus. Time stamps in (C), (D), and (F) indicate time since ablation. Asterisk indicates location of the stimulus. (**G**) Basal ablation triggered extrusion, unlike nuclear stimulation (data from 81 basal and 94 nuclear stimulations; $P < 10^{-23}$, Fisher's exact test). (**H**) Point ablation causes cell base expansion (magenta indicates before ablation; green indicates after). (**I**) Cell area expanded after basal but not nuclear ablation (Student's *t* test; data from 27 basal and 18 nuclear stimulations). (**J**) Basal expansion predicted extrusion (Mann-Whitney *U* test; 21 extrusions, 6 nonextrusions). (**K**) Basal expansion after ablation did not correlate with extrusion time (Pearson *r*, −0.14). (**L**) Confocal images of myosin-II (green) dynamics after basal point ablation. Asterisk indicates the location of the stimulus; arrowheads indicate the extruding cell. (**M**) Response to acute basal tension loss by laser-induced cytoskeletal ablation. (**N**) Blebbistatin reduced extrusion probability within 1 hour after basal ablation (Fisher's exact test; 81 control, 49 blebbistatin-treated organoids). (**O**) Vertical shift (ΔZ) over time (mean ± SEM of stimulated cells). (**P**) Extrusion time [Mann-Whitney *U* test; 22 extrusions per condition in (O) and (P)]. (**Q**) Multicellular junction ablation. Arrowheads indicate ablation site. [(F), (H), (L), and (Q)] Scale bar, 5 μm. (**R**) Ablation of multicellular junctions triggered extrusion of nearby cells (within 9 μm; $n = 34$ organoids). (**S** and **T**) Mosaic organoids with myosin II reporter (green) and H2B-iRFP–only cells (magenta). Time relative to spontaneous extrusion. Scale bars, 10 μm. (S) Extruding myosin reporter cell autonomous up-regulation of myosin. (T) Nonreporter cell extrusion induced myosin in neighbors. (**U**) myosin II levels over time in extruding cells (green) and their neighbors (magenta), aligned to extrusion. Data are from 10 extruding and 15 adjacent cells.

includes impaired intestinal barrier function, epithelial defects, and disrupted tissue organization, such as villous atrophy, crypt hyperplasia, and focal epithelial tufts (Fig. 7A) (*51*). These tufts are distinct histological features characterized by the disorganization and crowding of surface enterocytes into tuft-like structures.

To investigate the potential role of our proposed extrusion regulation mechanism in CTE, we introduced Epcam loss-of-function mutations in intestinal organoids using CRISPR-Cas9, generating three independent *Epcam*$^{-/-}$ lines (Fig. 7, B and C, and fig. S8A). Mutant organoids displayed distorted morphology: The well-structured morphology of WT organoids, characterized by distinct budding protrusions and a cystic center, was largely lost in *Epcam*$^{-/-}$ organoids (Fig. 7, C and D, and fig. S8, B and C). Time-lapse imaging of *Epcam*$^{-/-}$ organoids growing from small cystic organoids over several days revealed repeated cycles of inflation and deflation (movie S11). Compared to WT organoids, *Epcam*$^{-/-}$ organoids exhibited delayed budding, initiating bud formation after 3 rather than 2 days (Fig. 7E). Additionally, they grew into noticeably larger structures than WT organoids (fig. S8C). Using quantitative polymerase chain reaction (qPCR) and immunofluorescence, we confirmed that *Epcam*$^{-/-}$ organoids differentiated into all major intestinal lineages but exhibited some marked differences (fig. S8, D and E): Consistent with CTE's crypt hyperplasia, *Epcam*$^{-/-}$ organoids showed increased expression of markers for stem cells and immature enterocytes and a reduction in markers of mature cell types in comparison with WT organoids (fig. S8, D and E). These findings align with reports of delayed differentiation and persistent differentiation defects in CTE (*52*, *53*).

The reduced presence of mature cell types could be attributed to increased cellular turnover. To investigate this, we measured cell extrusion rates using a transwell assay and flow cytometry. *Epcam*$^{-/-}$ organoids exhibited a ~1.5-fold increase in extrusion rate compared with WT (Fig. 7F), and immunostaining for phospho–myosin II confirmed myosin hyperactivation (Fig. 7G and fig. S8, F and G). Our findings that excessive contractility and elevated tissue-level tension accelerated cell extrusion (Fig. 4, D and E) suggested that *Epcam* loss may contribute to epithelial dysregulation by increasing mechanical tension, which could promote premature cell removal and thereby manifest the disease phenotype.

To examine the effects of contractility differences in this disease-relevant context, we generated mosaic organoids containing WT and *Epcam*$^{-/-}$ cells and analyzed cell extrusion. Live imaging and quantification of extrusion enrichment revealed that hypercontractile *Epcam*$^{-/-}$ cells extruded less frequently, whereas WT cells were overrepresented among extruded cells. This effect became stronger with increasing abundance of *Epcam*$^{-/-}$ cells (Fig. 7, H and I, and fig. S8H). This mirrored our earlier finding with WT and opto-Arhgef11 cells, in which the less-contractile minority population was preferentially extruded (Fig. 5B). Combining two WT lines with different nuclear markers did not show such biased extrusion (Fig. 7J), confirming that contractility differences rather than genetic labels drive extrusion. To determine whether myosin II hyperactivation directly drives competitive extrusion, we inhibited Rho signaling pharmacologically using Y16 (Rho-GEF inhibitor) and Y-27632 (ROCK inhibitor) in mosaic *Epcam*$^{-/-}$/WT organoids with a majority of *Epcam*$^{-/-}$ cells. Both inhibitors significantly reduced WT extrusion enrichment, demonstrating that suppressing myosin II activity alleviates the extrusion bias against WT cells (Fig. 7K). Thus, tension heterogeneity within the epithelium drives cell extrusion, and differences in myosin II–mediated contractility create mechanical competition that determines which cells are extruded (fig. S9, A and B). This process, when dysregulated, may contribute to epithelial pathologies such as CTE.

Discussion

The self-renewal of the intestinal epithelium is commonly described with the analogy of a conveyor belt: Cells are continuously produced in intestinal crypts, move into the villus domain as they differentiate, and finally extrude into the lumen from the villus tip. In line with this model, it has been suggested that cells extrude in response to tissue crowding as they ultimately accumulate at the villus tip, where owing to the limited space, the tissue is compressed (*20*, *21*). Our findings challenge this model: Instead of tissue compression, we find that the basal surface of intestinal villi, including the tip region, is under tension. This tension is mediated by myosin II pulsations in the basal cytoskeleton, and cell extrusion rates are directly coupled to this tissue-level tension. Laser ablation of the cell base—causing local weakening—or genetic impairment of contractility both induce extrusion, suggesting that cells unable to sustain tension are eliminated. By contrast, (opto-)genetic activation of myosin II increases tissue-wide tension and amplifies the mechanical competition between cells, promoting the preferential extrusion of weaker cells. These complementary approaches reveal a shared principle: A cell extrudes when it can no longer sustain or reciprocate the tension exerted by neighboring cells—whether because of a local impairment of contractility or increased tension exerted by its neighbors.

In the intestine, an interconnected basal actomyosin network facilitates the transmission of physical forces throughout the villus epithelium, coordinating tissue-level behaviors such as cell extrusion, as shown here, but potentially also cell migration (*3*) and proliferation (*54*, *55*). Indeed, a cell's extrusion triggers cell contractility in its neighbors and impacts tissue-level tension. We propose a revision of the roles of cell extrusion and proliferation in tissue homeostasis. Cells at the villus tip are not pushed into crowding and compression but instead pull on their neighbors, driving a mechanical competition and leading to the preferential extrusion of less-contractile ("weak") cells. Thus, the intestinal epithelium acts as a self-renewing network of cells that autonomously replaces its weakest links. Indeed, cell extrusion thus not only serves to maintain cell number homeostasis but also to maintain "mechanical homeostasis"—the need to maintain and restore the optimal mechanical tissue state. Mechanochemical signaling dynamics driven by myosin II–mediated tissue tension thus complements biochemical signaling gradients in the organization and maintenance of intestinal homeostasis. This tissue-level tension caused by the extrusion of weak cells could, in turn, promote cell proliferation, and so proliferation may respond to extrusion to maintain cell number homeostasis, rather than driving extrusion. This would invert the conventional view of cause and effect in intestinal homeostasis. Indeed, increased tissue tension in intestinal organoids (*54*, *55*), MDCK monolayers (*56*), mouse colon (*57*), or the pig intestine (*58*) can stimulate cell proliferation.

Although the role of tensile basal actomyosin has been recognized in morphogenesis (*59*–*61*), we show its importance for intestinal barrier maintenance during tissue homeostasis. This has implications for pathologies in which the epithelial barrier function is impaired, beyond the tufting enteropathy studied here. For example, mutations in cytoskeletal components such as myosin IIA heavy chain (*62*), RAC1 (*63*), myosin IXB (*64*), keratin 8 (*65*), and cytoskeletal cross-linking protein ACF7 (*66*) are associated with increased epithelial permeability and are implicated in diseases characterized by excessive cell extrusion, such as inflammatory bowel disease (IBD, e.g., Crohn's disease and ulcerative colitis). By contrast, cancerous epithelial cells evade homeostatic cell extrusion and initiate primary tumors by distorting extrusion mechanisms and extruding through the basal rather than the apical surface (*67*, *68*). Mutation of RAS oncogenes—prime drivers of small intestinal adenocarcinomas (*69*)—interfere with myosin II activity and alter tissue mechanics [reviewed in (*70*)]. On the basis of our findings, we propose tissue tension as a potential therapeutic target that could be influenced through pharmacological modulation (*71*) to alleviate excessive shedding in the context of IBD or to accelerate the extrusion of cells that threaten intestinal integrity, e.g., during pathogen infections (*72*–*74*).

Materials and methods

Organoid culture

Organoids were grown in basement membrane extract (BME; Biotechne R&D Systems; cat. #3533-010-02) and ENR growth medium. ENR growth medium was prepared with murine recombinant Noggin (100 ng/ml; Thermo Fisher, cat. #250-38-100UG) and human recombinant R-spondin 1 (500 ng/ml; Thermo Fisher, cat. #120-38-5UG), 1 mM n-acetylcysteine (Merck, cat. #A9165-5G), 50 ng/ml epidermal growth factor (EGF; Thermo Fisher cat. #315-09-500UG), N2 and B27 supplement (1×; Thermo Fisher, cat. #17502048 and #17504044, respectively), Glutamax (2 mM; Thermo Fisher cat. #35050061), HEPES (10 mM; Thermo Fisher, cat. #15630080), 100 U/ml Penicillin, 100 μg/ml Streptomycin (Penicillin-Streptomycin, Gibco Thermo Fisher Scientific, cat. #11548876) in Advanced DMEM/F12 (Thermo Fisher, cat. #12634010). Passaging was done once

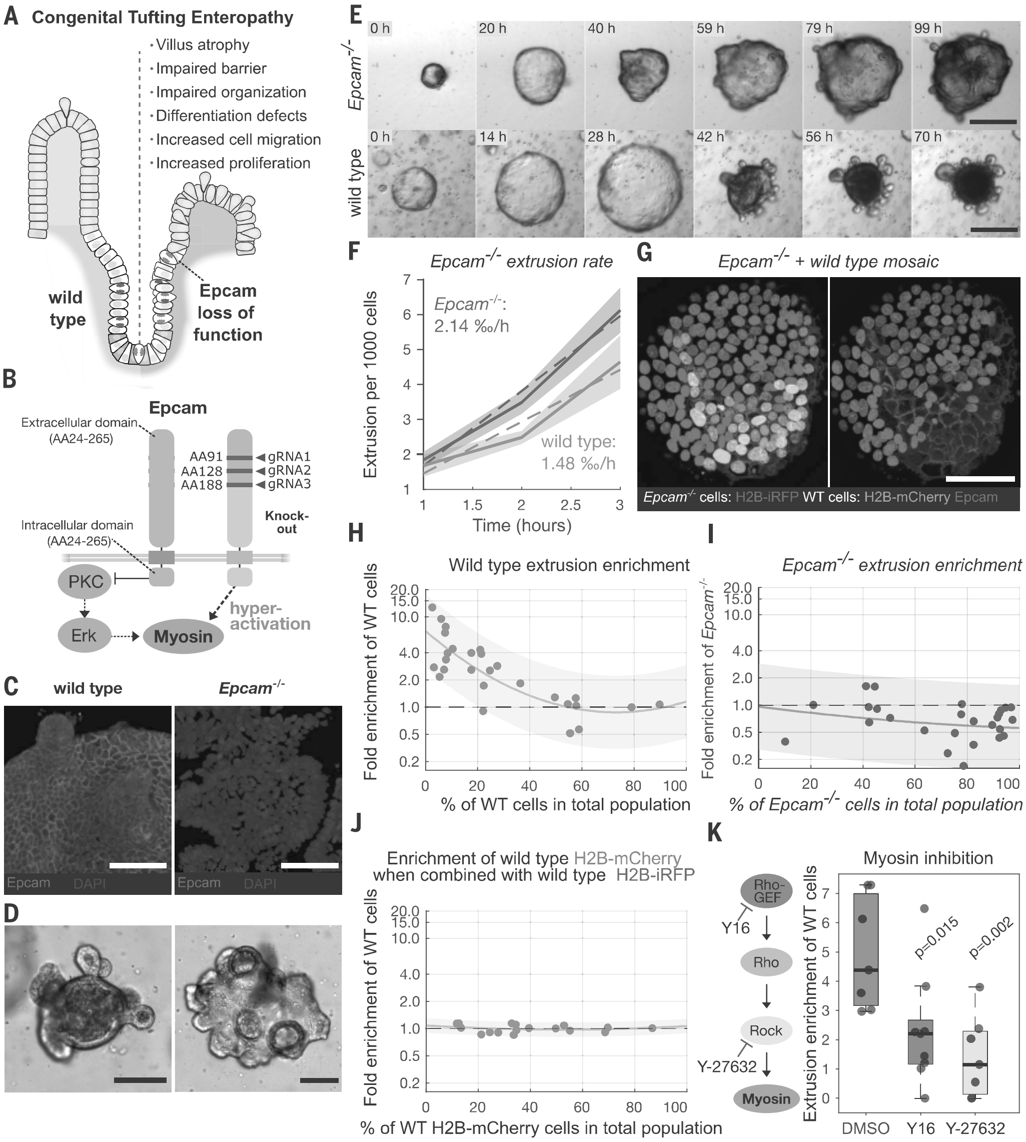

Fig. 7. Hyperactivation of myosin II in *Epcam*$^{-/-}$ cells disrupts epithelial homeostasis and drives competitive cell extrusion. (**A**) Hallmarks of congenital tufting enteropathy (CTE), a disease caused by loss-of-function mutations in *Epcam*. (**B**) Schematic of Epcam function and its role in myosin II inhibition. (Right) CRISPR-Cas9 strategy to generate *Epcam*$^{-/-}$ organoids (guide sites shown). Epcam loss leads to myosin II hyperactivation. (**C** and **D**) Immunofluorescence staining [Epcam (magenta) and DAPI (blue)] and brightfield images of WT and *Epcam*$^{-/-}$ mutant organoids. Scale bars, 50 μm (C) and 100 μm (D). (**E**) Brightfield images showing growth and morphological changes of WT (bottom) and *Epcam*$^{-/-}$ (top) organoids over time. Scale bars, 100 μm. (**F**) Quantification of cell extrusion rates using a transwell assay and flow cytometry; *Epcam*$^{-/-}$ organoids (red) show a significantly higher extrusion rate compared with WT (green). The solid line shows the mean, the dashed line shows linear fit, and the shaded area shows the SEM data: 5 WT, 12 *Epcam*$^{-/-}$ [5 of a mutant line generated with guide RNA1/2 (gRNA1/2); 2 of a line generated with gRNA3] transwells. (**G**) Immunofluorescence for Epcam (magenta) in a mosaic organoid with H2B-iRFP–labeled Epcam cells (also magenta) and H2B-mCherry–labeled WT cells (green). Scale bar, 50 μm. (**H** and **I**) Extrusion enrichment in mosaic organoids composed of H2B-iRFP–labeled *Epcam*$^{-/-}$ cells and H2B-mCherry–labeled WT cells. Extrusion enrichment of WT (H) or *Epcam*$^{-/-}$ (I) cells is shown at varying fractions of the respective cell population in the mosaic organoid. WT cells become increasingly enriched among extruded cells as the proportion of *Epcam*$^{-/-}$ neighbors rises, whereas *Epcam*$^{-/-}$ cells are underrepresented (27 organoids). (**J**) Extrusion enrichment in control mosaics with WT cells labeled by different nuclear markers showed no bias. [(H) to (J)] Each dot indicates one organoid; exponential fit ± 95% CI (shaded). The *y* axis shows the log scale. (**K**) Pharmacological inhibition of Rho signaling upstream of myosin II activity with Y16 or Y-27632 (scheme on left) reduces extrusion enrichment of WT cells in WT/*Epcam*$^{-/-}$ mosaics. Data are from seven DMSO-treated, nine Y16-treated, and seven Y27632-treated organoids; two-sided Student's *t* test.

and the medium change twice per week on non-consecutive days. During passaging, BME was dissolved in cold base medium (2 mM Glutamax, 10 mM HEPES in Advanced DMEM/F12) and organoids were mechanically disrupted, before embedding in new BME and plating onto a culture plate. BME was left to solidify for 20 to 30 min before new growth medium was added. For expansion and outgrowth of single cells, organoids were cultured in Wnt-conditioned medium [ENR, 10 mM Nicotinamide (Sigma-Aldrich, cat. #98-92-0), home-made Wnt3A conditioned medium 50% (v/v) (*75*)]. Organoids expressing the optogenetic module were kept in the dark in an aluminum vessel. To inspect optogenetic organoids, culture plates and dishes were placed in containers wrapped in Deep Amber lighting filter foil (Cabledelight) to filter blue light.

Cloning

Gibson Assembly (NEBuilder HiFi DNA Assembly, NEB, cat. # E2621) was used for the cloning of all constructs. Transgenic constructs were cloned into p2T vectors that flank the inserts with 3′ and 5′ tol2 sequences. These transposable elements mediate the mT2TP transposase-dependent random integration of the expression constructs into the cell genome. For p2T-CIBN-GFP-PuroR, a new p2T vector was assembled by combining fragments containing an empty p2T backbone, the CAG promoter, CIBN-GFP [from (*76*)] and IRES-PuroR. To express Arhgef11-CRY2 under Dox-inducible promoter, in a p2T backbone, the Tet-ON 3G transcription factor driven by a CMV promoter [from (*77*)] was combined with a P2T-T2T tandem and a HygromycinR. In opposite direction, a TRE3GS promoter [from (*77*)] was cloned to drive the PHR-CRY2 domain fused to Arhgef11 (from Addgene plasmid #89481) and followed by a SV40 polyA tail. A second construct containing Argef11-mCherry-CRY2 was generated based on the p2T-TetON-Hygro-Arhgef11-CRY2 construct. For p2T-H2B-iRFP-IRES-PuroR and p2T-H2B-mCh-IRES-BlastR nuclear markers, the p2T-CIBN-GFP-BlastR construct was cut with XhoI and BsrGI (both New England Biolabs, cat. #R0146S, #R3575S) and fragments containing H2B, iRFP670 or mCherry and IRES-BlasticidinR were combined. p2T-CMV-H2B-eGFP-SV40-HygroR was assembled to contain the p2T backbone, a CMV promoter driving H2B-mEGFP and a SV40 promoter driving a HygromycinR. 2 CRISPR-HOT donor plasmids were generated. Based on pCRISPaint-mNeon (Addgene plasmid #174092), new donors containing pCRISPR-HOT-mNeon-P2A-T2A-mCherry-CAAX (to generate mNeonGreen fusion protein that co-translates a red-fluorescent plasma membrane marker), pCRISPR-HOT-mNeon-Stop-PGK-mCherry-CAAX (to generate mNeonGreen fusion protein and expresses a red-fluorescent plasma membrane marker independently under the PGK promoter) were generated using Gibson assembly.

CRISPR-mediated reporter and knockout generation

Knock-in reporter organoids were generated using CRISPaint technology (*78*) and the CRISPR-HOT method (*79*). A gene-specific sgRNA-containing plasmid (Table S1) was co-transfected (*80*) with a donor plasmid containing the fluorescent tag and the frame-selector plasmid containing an sgRNA to linearize the donor plasmid and the Cas9 into mouse intestinal organoids (each 5 μg sgRNA plasmid) using a NEPA electroporation system (NEPAGENE). Myosin knock-in reporter organoids were generated using both pCRISPR-HOT_mNeon-P2A-T2A-mCherry-CAAX and pCRISPR-HOT_mNeon-Stop-PGK-mCherry-CAAX donor vectors. The comparison of the target-specific co-expression and independent expression of the mCherry plasma membrane marker allowed an estimation of signal strength and localization across gene targets. Myl12a-mNeonGreen-P2A-T2A-mCherry-CAAX was selected to characterize myosin activity and dynamics in organoid tissue. In addition, pCRISPR-HOT_tdTomato (Addgene plasmid #138567) was used to generate a Myl12a-tdTomato line and pCRISPaint-mNeon in combination with a Cdh1-specific sgRNA was used to generate a live reporter for E-cadherin. 3 days before and 2 weeks after electroporation organoids were split and cultured in Wnt-conditioned medium. Expression of fluorescent reporters in individual organoids was monitored daily. To generate stable organoid lines, fluorescent organoids were picked, dissociated to single cells using TrypLE Express Enzyme (Thermo Fisher Scientific, cat. #12605010) and expanded for 2 weeks in Wnt-conditioned medium. Stable lines were cultured in ENR medium.

For gene-specific knockout generation, a sgRNA vector conferring a transient Hygromycin and a Cas9 vector conferring a transient Puromycin resistance were co-transfected. After electroporation organoids were cultured in Wnt-conditioned medium. 1 day after electroporation the organoids were exposed to Puromycin (2 μg/ml; InvivoGen, cat. #ant-pr) and Hygromycin B Gold (100 μg/ml; InvivoGen, cat. #ant-hg) for 24 hours. 2 weeks after electroporation outgrown organoid clones were picked, dissociated to single cells, DNA was extracted using Quick-DNA Microprep Kit (Zymo Research Corporation, cat. #D3021) and genotyped using gene-specific primer pairs (sanger sequencing performed by Macrogen Europe BV). Clonal organoid lines were cultured in ENR medium.

Generation of transgenic organoids

Organoid lines expressing H2B nuclear marker (*30*, *81*), Dox-inducible optogenetic modules and the optogenetic anchor CIBN-GFP were generated by co-electroporation of 5 μg of the respective expression construct and 5 μg of a vector containing the mT2TP transposase driven by the CAG promoter for the transient expression of mT2TP mediating the tol2-dependent genome integration of expression constructs. 1 week after electroporation organoids were exposed to the expression construct-conferred resistance. The culture was propagated and maintained in ENR medium containing the expression construct-conferred resistance.

Sample preparation of synthetic hydrogels with crypt-villus topology

ECM-based hydrogel substrates were generated as described previously (*8*). Before organoid seeding, the substrates attached to 35-mm culture dishes were sterilized using UV illumination and repeated washes using PBS solution containing Primocin (1:500; InvivoGen, cat. #ant-pm) and incubated in Wnt-conditioned medium overnight. Cells were incubated in Wnt-conditioned medium 3 days before seeding. For cell seeding, BME was enzymatically digested using Dispase (Stemcell Technologies cat. #07913) and washed away using cold base medium. Cells were dissociated to single cells using Accutase Cell Detachment Solution (Innovative Cell Technologies, cat. #AT104-500), pelleted by centrifugation at 250×g for 5 min and resuspended in 15 μl of Wnt-conditioned medium. Medium was aspirated from substrates and the cell suspension was seeded evenly onto the surface. Cells were allowed to attach for 5 min at 37°C before more Wnt-conditioned medium containing 10 μM Y-27632 (Abmole, cat. #M1817) was added to fill the culture dish. The cells were kept in Wnt-conditioned medium for 4 days, in Wnt-conditioned medium diluted 1:2 in ENR for 3 days and eventually kept in ENR medium. Organoids expressing the optogenetic modules were kept in medium containing Puromycin (1 μg/ml) and Hygromycin B Gold (100 μg/ml) and incubated in a dark aluminum chamber and inspected through blue-light filtering foil.

Generation of mosaic organoids

Organoid lines were dissociated to single cells as described for seeding on hydrogel substrates, resuspended in Wnt-conditioned medium and combined at desired ratios. The cell suspension containing 300,000 cells in 20-μl medium was mixed well by repeated pipetting and 20 μl were seeded per well onto a 48-well plate. The plate was spun at 200×g for 5 min and incubated for 30 min at 37°C before Wnt-conditioned medium (with 10 μM Y-27632) was added. After 24 hours the cell layer was mechanically detached by scraping off the cell layer using a pipette tip and repeated flushes with base medium. Without extra mechanical sheering, the cells were collected by centrifugation and seeded directly into microscope sample carriers. Organoids were cultured in ENR medium. Mosaic organoids were imaged for 12 to 20 hours using a Leica Stellaris confocal microscope or Viventis Light sheet microscope.

Extrusion measurement of *Epcam*$^{-/-}$ and WT cells

Transwell inserts with 0.1-μm pore size (Corning, cat. #CLS3396) were coated with 5% BME for 30 min. Organoid cells were dissociated into single cells as described above, resuspended in Wnt-conditioned medium supplemented with 10 μM Y-27632, and seeded onto the transwell surface at a density of 200,000 cells per insert. The cells were cultured for 4 days in Wnt-conditioned medium to achieve full confluency, followed by 2 days in transition medium (1:1 mix of ENR and Wnt-conditioned medium). To promote differentiation, monolayers were then maintained for 10 days in ENR medium. Only transwells with complete and confluent monolayer coverage were included in downstream analysis. Flow cytometry was used to count extruded cells in the medium covering the monolayer. To this end, the medium covering the monolayer was refreshed and collected after 1, 2, and 3 hours. The cells were stained with DAPI (1 μg/ml) and the number of extruded cells was measured by FACS using a CytoFLEX (Beckman Coulter). To normalize extrusion rates to the number of cells in the monolayer, the transwell membranes were fixed in 4% paraformaldehyde for 30 min at room temperature, washed with PBS, and stained with DAPI (1 μg/ml). Whole-membrane tile scans were acquired using a Leica Thunder widefield microscope with a 5× air objective. Cell nuclei were segmented using StarDist in Fiji, and total cell numbers were quantified. The extrusion rate was calculated as the number of extruded cells (by FACS) divided by the total number of monolayer cells (by image segmentation), normalized to the time of sample collection.

Long-term live-cell imaging and image analysis

For long-term live imaging of nuclear reporter organoids, organoids were seeded onto an imaging chamber (CellVis 4 Chambered Coverglass System cat. #C4-1.5H-N) and imaged on a A1R MP (Nikon) scanning confocal microscope outfitted with a 1.30 NA 40× magnification oil immersion objective, incubation chamber set to (37°C, 5% CO_2) (*30*). Images were taken every 12 min, and at each time point, 31 Z-slices were imaged with 2-μm intervals.

For live imaging of organoids grown on synthetic crypt-villus substrates, the chips were placed into a μ-Dish 35 mm glass bottom dish (Ibidi, cat. #81218-200) onto a circular holder made of PDMS material with a width of ~2 mm. The samples were imaged using a Leica SP8 confocal microscope using a HC PL APO CS2 20x/0.75 air objective at 37°C and 5% CO_2. Z-Stacks of 40 μm were collected with 1 μm Z-interval and with a time interval of 6 min.

Epcam$^{-/-}$ and WT organoids were seeded on a 96-well glass bottom plate and imaged over a period of 1 week using a Leica Thunder widefield microscope using a 5× air objective and brightfield illumination.

Cell tracking

Semi-automated tracking of single cells and their extrusion from organoids was done by tracking the cell nuclei using the OrganoidTracker (*29*) software. Tracks and lineage trees were analyzed in Python. Cells were censored when they moved out of view or were still alive when the image acquisition was stopped. We measured the cell density around a cell as the inverse of the average distance to its 6 closest neighbors (in millimeters), using the *cell_density_calculator* in OrganoidTracker (*29*).

Optogenetic experiments

Photoactivation of opto-Arhgef11 organoids was done using a Leica SP8 confocal microscope using a HC PL APO CS2 40×/1.10 water objective. 3D organoids expressing the system were imaged first using only 640-nm excitation to collect transmitted light and the H2B-iRFP nuclear marker signal (pre-activation). For regional photoactivation a region of interest (ROI) was designed, which was set to be illuminated with low intensity of 488-nm light (0.5 to 1%). A time course with a time interval of 1 s was started with simultaneous illumination of the entire organoid with 640-nm excitation (to collect transmitted light and the H2B-iRFP nuclear marker signal) and 488-nm photoactivation specific to the ROI. In this region, the GFP signal of the labeled optogenetic anchor was recorded. To stop photoactivation, the laser power of the 488-nm laser was set to zero. To record the translocation of Arhgef11-CRY2-mCherry to the plasma membrane, a Zeiss LSM780 was used with a C-Apochromat 40×/1.20 W Korr M27 water objective (Zeiss). First, the mCherry signal was collected using 564-nm excitation, then a region was illuminated within a ROI using 488-nm illumination and the mCherry signal was collected again after 5 s. For the photoactivation of optogenetic organoids grown on synthetic hydrogels, a Leica SP8 confocal microscope using a HCX IRAPO L 25×/0.95 water objective was used. A water pump was attached to the water immersion objective that compensated for water evaporation during the experiments. As a control, we first imaged optogenetic organoids on hydrogel substrates that were not induced by doxycycline before for 2.5 hours at a time interval of 4 min with both 640-nm light to record the H2B-iRFP nuclear signal and 488-nm blue light. The positions of the imaged villi were saved. Afterwards the organoids were incubated for 12 hours to let them recover, induced with 1 μg/ml doxycycline (Thermo Fisher Scientific, cat. #10592-13-9) for 24 hours and the same villi were imaged for 2.5 hours only with 640-nm light without 488 nm. Again, the organoids were incubated for 12 hours and the villi were imaged for 2.5 hours with both 640 nm and photoactivated using 488-nm light. Extrusions were counted and the extrusion rates were calculated for each villus. In another setup, the samples were first imaged for 2.5 hours exclusively with 640-nm light (non-activation), followed by 2.5 hours with simultaneous photoactivation using 488-nm light in time intervals of 4 min. For patterned photoactivation of only one half of the villus tip, the tip was first centered and imaged in the full field of view using 640-nm light, while the left half was selectively illuminated with 488-nm light for 2.5 hours. Mosaic organoids were imaged using a Leica Stellaris Confocal microscope using a 20× air objective (20×/0.75 Air, Leica) or using a Viventis Light sheet microscope, as described below, and photoactivated every 5 min. For all optogenetic experiments: To be able to position the optogenetic samples at confocal microscopes a deep Amber lighting filter foil (Cabledelight) was placed on top of the condenser to block blue light from brightfield illumination.

Light-sheet imaging

Live imaging of Myo-mNG reporter organoids and mosaic organoids was performed using a LS1 Live light sheet microscope (Viventis Microscopy) using a Nikon 25× NA 1.1 water immersion objective at a magnification of 18×. Organoids were mounted on a single-chamber sample holder 1 day before the start of imaging. Organoids were imaged at 37°C and 5% CO_2. A position-specific alignment of the light sheets with a thickness of 2.2 μm was done. Organoids were imaged every 8 min using appropriate laser lines depending on the fluorophores expressed. Myo-mNG reporter organoids were imaged with 488-nm and 561-nm illumination. Mosaic organoids expressing combinations of H2B-mCherry, H2B-iRFP, H2B-GFP, or CIBN-GFP were imaged using 561-nm, 638-nm, and 488-nm illumination, respectively. Organoids co-expressing Myo-mNG with H2B-iRFP, or Myo-tdTomato with H2B-GFP and H2B-iRFP, were imaged using 488-nm and 638-nm, or 488-nm, 561-nm, and 638-nm illumination, respectively. Post-acquisition analysis was performed using Fiji.

Image analysis of short-term movies

Image processing and analysis was done using Fiji (*82*)/ImageJ2 (*83*). To measure the basal expansion after laser-ablation of the basal cytoskeleton, organoids expressing H2B-mCherry and E-cadherin-mNeonGreen were plated onto an imaging plate (day 0) and ablated at the base on day 2. The time-lapse video of the stimulation was taken from 5 s before stimulation until 15 s after stimulation, and the basal area of the ablated cells was measured on the average E-cadherin-mNeonGreen signal before (-5 s < t < 0 s) and after (10 s < t < 15 s) ablation. 3D renderings were generated by exporting nuclei positions from OrganoidTracker and rendering in ParaView (v. 5.11.0).

The basal surface of reporter organoids grown on synthetic crypt-villus substrates was extracted using the Fiji plugin LocalZProjector (*84*). Basal cell membranes were segmented and tracked manually using Napari (napari.org) and analyzed in Matlab (2021b, MathWorks). Myosin levels were quantified using Matlab by creating binary masks for individual cells and time points to calculate the cell area and mean fluorescent signal. Graphs were visualized using the *plot* function and smoothened with a factor of 3. To identify myosin or basal area peaks (primary parameter), a trend curve was calculated and subtracted from the raw signal before maxima were identified using the *findpeaks* function. To calculate the trend, a polynomial function of 4th degree was fitted to single cell myosin/basal area curves (signal over time) using the *fit* function. The corresponding secondary parameter was analyzed and averaged across all identified signal peaks within a defined time window (typically 1 hour) centered around each peak to generate the final graph. 3D rendering of organoids growing on hydrogels with crypt-villus topology was done using Imaris 10.0 (Oxford Instruments).

To quantify apical and basal myosin levels, crypts recorded in the cross section were selected and a line was drawn following the shape of the epithelium with ~150-μm length. The epithelium was virtually transformed into a straight line using the Fiji *straighten* function. A line was drawn on the apical and basal surface respectively and the signal measured with a line width of 4 μm to obtain the respective line profiles. Line profiles centered around multiple crypts were averaged and depicted in the final graph. The same approach was used to measure the apical and basal myosin profile for a single developing crypt over time. To this end, for each time point the shape of the epithelial line was adjusted and the measured distances scaled to match the length of the final crypt-villus region.

To analyze extrusion of cells upon optogenetic activation of myosin, the acquired H2B-iRFP nuclear marker signal was used to monitor cell dynamics. The detection of cell extrusion events and total cell counts were done using the Fiji plugin *Cell Counter* and the position and time were registered. Counting was done in a blinded fashion without information about the photoactivation pattern by a person, who was not the experimenter. Using Matlab, the positional and temporal data were analyzed. To analyze the extrusion rate over time, it was calculated as the average number of extrusions per total cells within a 25-min time window. To analyze the position of extruding cells, the position data of extrusion events and total cells were binned equally using the *hist3* and visualized using the *imagesc* function. The x- and y-profile for cell extrusions and total cells was generated by calculating the mean density along the respective axis within a 9-μm window. The raw extrusion profile was then normalized by the total cell profile to obtain the final extrusion profile.

For the quantification of mosaic organoids, the respective cell population was measured as fraction of the total and extruded cell population (extrusion enrichment), extrusions and total cells were manually counted based on the co-expressed fluorescent markers using Napari and Fiji Cell counter. Counting was done in a blinded fashion. Mosaic organoids were excluded from analysis if they showed no extrusions, moved out of focus, exhibited excessive damage, or had insufficient signal strength during imaging.

Immunofluorescent staining of whole-mount intestinal tissue

Mice were sacrificed and the small intestine was dissected. The lumen was flushed several times with cold PBS. The tissue was cut as a tube and opened along the longitudinal axis. The tissue was fixed in 4% paraformaldehyde solution at 4°C overnight and washed with PBS. The cells were permeabilized using 2% PBST (2% Triton X-100 in PBS) for 2 days at room temperature and washed with PBS. The sample was incubated in blocking buffer (10% normal goat serum, 1% Triton-X 100, 2.5% DMSO in PBS) for 2 days at 4°C. The sample was incubated in primary antibody solution (1% normal goat serum, 0.2% Triton-X 100, 2.5% DMSO, and 0.2% sodium azide in PBS; rabbit anti-myosin light chain (phospho S20) antibody (Abcam, cat. #ab2480) diluted 1:200), incubated for 5 days at 4°C and washed with PBS at room temperature. The sample was incubated in secondary antibody solution [1:500 goat anti-rabbit IgG Alexa-488 (Thermo Fisher Scientific, cat #A-11008) and 1:1000 phalloidin-atto647N (Sigma-Aldrich, cat. #65906)] for 2 days at 4°C and washed in PBS. The sample was stained with DAPI (1 μg/ml) diluted in PBST 4°C overnight. The sample was cleared with RapiClear 1.47 Solution (SunJin Lab, cat. #RC147001) overnight at 4°C. The sample was placed on a glass-well plate and imaged using a Leica Stellaris confocal microscope using a HC PL APO CS2 20×/0.75 air objective (Leica) for overview images (voxel size: 0.28 by 0.28 by 0.69 μm^3) and a HC PL APO CS2 63×/1.40 oil objective (Leica) for high-resolution image stacks (voxel size: 0.0586 by 0.0586 by 0.2985 μm^3). For the quantification of basal myosin level along the villus, villi that were located longitudinally to the objectives were imaged and stacks were recorded. Using Fiji, a Z-profile was generated using the *reslice* function and a line was drawn below the nuclei at the basal surface. The line profiles of several villi were overlayed relative to the distance to the villus tip.

Whole-mount organoid staining

Organoids were fixed in 4% paraformaldehyde for 30 min at room temperature, washed in PBS, blocked in blocking solution (PBS; 0.5% Tween, 5% normal goat serum) for 1 hour at room temperature and stained overnight with primary antibodies in antibody solution (PBS; 0.1% Tween, 1% normal goat serum). Primary antibody used for phosphor–myosin II staining: Rabbit anti-mouse phospho-myosin light chain 2 (Thr18/Ser19) (Cell Signaling Technology, cat. #3674). Primary antibody used for Epcam staining: Rat anti-mouse CD326-APC (Clone G8.8) (eBioscience, cat. #17-5791-80). After washing in PBS, organoids were stained with secondary antibody (Goat anti-Rabbit IgG Alexa-488, Invitrogen, cat. #A-11008) in antibody solution for 1.5 hours at room temperature. After washing in PBS, organoids were stained with DAPI (1 μg/ml) in PBS for 15 min and mounted on glass slides.

STED super-resolution microscopy

Organoids were fixed in 4% paraformaldehyde for 30 min at room temperature, washed in PBS, blocked in blocking solution (PBS; 0.5% Tween, 5% normal goat serum) for 1 hour at room temperature and stained overnight for phalloidin conjugated to the STED fluorophore atto647-N. The organoids were washed and incubated for 10 min at room temperature in PBS containing DAPI (1 μg/ml). Organoids were mounted in ProLong Gold Antifade Mountant (Molecular Probes/Thermo Fisher Scientific, cat. # P10144) medium on a glass carrier. A 0.16- to 0.19-mm-thick (thickness 1.5) cover glass (Glaswarenfabrik Karl Hecht GmbH & Co KG, cat. #41014) was placed on top, and excessive mounting medium was removed using tissue paper, dried, and sealed using nail polish. 2D-STED image stacks were collected using a Leica Stellaris 8 STED microscope with a HC PL APO CS2 100×/1.40 oil objective and type F immersion liquid. The phalloidin-atto647N–stained sample was imaged combining 650-nm excitation with the 775-nm STED depletion laser. The image was scanned with a voxel size of 0.0199 by 0.0199 by 0.1826 μm^3, a line accumulation of 16, a dwell time of 0.75 μs. Sequentially the myosin-mNeonGreen reporter and DAPI signal was collected in the classical confocal mode.

Animal work

Mice were maintained by professional caretaker according to procedures approved by the Central Committee Animal Experimentation (CCD) of the Dutch government and approved by the KNAW/Hubrecht Institute Animal Welfare Body (IvD). Mouse strain (*Mus musculus*): C57BL6/J, male and female of age 7 to 12 weeks without genetic modifications (RRID:IMSR_JAX:000664) was used.

Laser ablation in the living mouse intestine

Mice were sacrificed and immediately afterwards the intestine was dissected in ice-cold PBS-Orange containing CellMask Orange Plasma Membrane Stain (Invitrogen/Thermo Fisher Scientific, cat. #C10045) diluted 1:1000 and Primocin (InvivoGen; 1:500) in PBS. The lumen was flushed several times with ice-cold PBS-Orange. The musculature and connective tissue outside the intestinal tube was removed as much as possible. The intestine was cut open, inverted, and placed onto a glass-bottom well with a cover glass on top to bring the sample closer to the objective. The well was filled with ENR medium containing CellMask Orange (1:1000) and Primocin (1:500). A Leica SP8 confocal microscope equipped with a tunable Chameleon multiphoton laser with a HC PL IRAPO 40×/1.10 water objective (Leica) was used at room temperature and 5% CO_2. The objective was positioned at villus regions, and the cell base identified. Laser ablation using a wavelength of 800 nm of the Chameleon laser was done with a 1-pixel wide and 15-μm long line with 80% laser intensity for three iterations. Before laser ablation 10 and after ablation 30 frames were collected with a time interval of 1 s. Per mouse sample multiple positions at the villus tip and villus shaft were processed. The procedure from dissection to laser ablation was optimized to not exceed a duration of 1.5 hours. To analyze tissue recoil, the Euclidean distance from the initial position was manually tracked for at least 10 cell interfaces on both sides of the ablation line. The mean recoil for each ablation experiment was calculated, and the average across multiple experiments was presented in the final graph. The initial recoil velocity was calculated by fitting a sigmoidal curve (with A: amplitude, k: steepness, t_0: inflection point, y_0: vertical offset) to each experiment and the slope of the curve at the inflection point (v_{initial}) was calculated:

$$f(t) = \frac{A}{1 + e^{-k(t - t_0)}} + y_0$$

$$v_{initial} = f'(t_0) = \frac{A \cdot k}{4}$$

To ablate individual cells along their apical-basal axis, villus tip regions were selected where tissue orientation allowed a ~30-μm line cut through the full length of a single cell, using the same laser settings as described above. The boundaries of the targeted cell were segmented, and all experiments were aligned by normalizing cell dimensions prior to ablation. Average cell shapes before and after ablation were calculated, and boundary displacement vectors were computed based on these contours.

To quantify orthogonal recoil upon laser ablation in crypt-villus substrates, synthetic tips were photoactivated with 488-nm light for 1 hour at 5-min intervals and compared to non-activated controls. Recoil was measured by tracking H2B-iRFP–labeled nuclei along the ablation line and determining their maximal displacement within 30 s post-ablation.

Laser point ablation

For the laser point ablation experiments, organoids were seeded onto an imaging chamber (CellVis) and imaged on a Nikon A1R MP scanning confocal microscope using a 1.30 NA 40× magnification oil immersion objective, and the incubation chamber was set to (37°C, 5% CO_2) (*30*). For each time point, 31 Z-slices were imaged with 2-μm intervals. We only selected organoids that contained at least one crypt and a villus domain. An 8-ms laser stimulus of 800-nm wavelength was applied (MaiTai DeepSee, 100% laser power), which was optimized such that epithelial barrier integrity was maintained while still triggering cell extrusion. Time-lapse videos for laser stimulation were acquired at more than 2 frames/s. Only one ablation was done per organoid and organoids were subsequently imaged for at least 1 hour to determine if a stimulated cell extruded. Ablated organoids were excluded from analysis if (i) the stimulus missed the organoid (i.e., if no visible bleaching of the nucleus occurred and/or no cavitation bubble was observed when stimulating the cytoskeleton), (ii) imaging failed within 1 hour after stimulation, (iii) ablated cells extruded to the basal side in response to the ablation. Determination of the region (base/nucleus/junction) in which cells were ablated was determined as follows: If a cavitation bubble was observed below the nucleus, a cell was classified as ablated at the base. If no cavitation bubble was observed, but the nucleus was partially bleached, the cell was classified as ablated in the nucleus. If a cavitation bubble was observed in the same *xy*-plane as the nucleus but a cavitation bubble was observed outside the nucleus, the stimulation was classified as a stimulation of a multicellular junction. Whether cells extruded (within 1 hour) in response to point ablation was determined by visual inspection. To determine the extrusion time of cells that extruded in response to the point ablation, we tracked the nuclei of the extruding cells and their immediate neighbors for 1 hour. For single-cellular extrusions, we computed the relative vertical displacement of the extruding cells from their non-extruding neighbors (ΔZ) as follows:

$$\Delta Z = Z_i - \frac{1}{|\Omega_i|} \sum\nolimits_{j \in \Omega_i} Z_j$$

where Ω_i is the set of neighbors of extruding cell i. For multicellular extrusions, we computed ΔZ as:

$$\Delta Z = \overline{Z}_{ext} - \frac{1}{|\Omega|} \sum\nolimits_{j \in \Omega} Z_j$$

where $\overline{Z}_{ext}$ is the average Z-level of all the co-extruding cells, and Ω is the set of all non-extruding neighbors of all extruding cells. Extrusion time was defined as the time until $\Delta Z > 5$ μm.

Real-time qPCR

Total RNA was extracted from control and *Epcam*$^{-/-}$ organoids using the RNeasy Mini Kit (Qiagen), following the manufacturer's protocol. RNA concentration was determined spectrophotometrically and diluted to a uniform concentration. cDNA was synthesized from 540 ng total RNA using the High-Capacity RNA-to-cDNA Kit (Applied Biosystems, cat. #4388950). qPCR was performed using SYBR Green Supermix (Bio-Rad, cat. #1725121) in 384-well format with gene-specific primers (table S2) and 4 ng of cDNA per reaction. The cycling protocol consisted of an initial denaturation at 95°C for 3 min, followed by 40 cycles of 95°C for 10 s, 60°C for 30 s, and 72°C for 30 s. Fluorescence was recorded after each cycle. Average CT values were calculated from technical duplicates and normalized to the geometric mean of *Actb* and *Gapdh*. Relative gene expression levels were determined using the ΔΔCT method and normalized to control organoids.

Pharmacological treatments

For the laser ablation of blebbistatin-treated organoids, the organoids were incubated overnight in ENR medium supplemented with 100 μM (±)-blebbistatin (Abcam, cat. #120425). For measuring extrusions in mosaic *Epcam*$^{-/-}$ organoids, organoids were pre-incubated for 5 hours in 50 μM Y-16 (MedChemExpress, cat. #HY-12649) and 10 μM Y27632 (AbMole, cat. #M1817) and imaged for 16 hours.

Statistical analysis

Statistical tests were done using the scipy.stats library (*85*) and the Matlab Statistics and Machine Learning Toolbox (Mathworks).

REFERENCES AND NOTES

1. A. S. Darwich, U. Aslam, D. M. Ashcroft, A. Rostami-Hodjegan, Meta-analysis of the turnover of intestinal epithelia in preclinical animal species and humans. *Drug Metab. Dispos.* **42**, 2016–2022 (2014). doi: 10.1124/dmd.114.058404; pmid: 25233858
2. N. Barker, Adult intestinal stem cells: Critical drivers of epithelial homeostasis and regeneration. *Nat. Rev. Mol. Cell Biol.* **15**, 19–33 (2014). doi: 10.1038/nrm3721; pmid: 24326621
3. D. Krndija *et al.*, Active cell migration is critical for steady-state epithelial turnover in the gut. *Science* **365**, 705–710 (2019). doi: 10.1126/science.aau3429; pmid: 31416964
4. A. G. Schepers, R. Vries, M. van den Born, M. van de Wetering, H. Clevers, Lgr5 intestinal stem cells have high telomerase activity and randomly segregate their chromosomes. *EMBO J.* **30**, 1104–1109 (2011). doi: 10.1038/emboj.2011.26; pmid: 21297579
5. N. Barker *et al.*, Identification of stem cells in small intestine and colon by marker gene Lgr5. *Nature* **449**, 1003–1007 (2007). doi: 10.1038/nature06196; pmid: 17934449
6. T. Sato *et al.*, Single Lgr5 stem cells build crypt-villus structures in vitro without a mesenchymal niche. *Nature* **459**, 262–265 (2009). doi: 10.1038/nature07935; pmid: 19329995
7. T. Sato *et al.*, Paneth cells constitute the niche for Lgr5 stem cells in intestinal crypts. *Nature* **469**, 415–418 (2011). doi: 10.1038/nature09637; pmid: 21113151
8. N. Gjorevski *et al.*, Tissue geometry drives deterministic organoid patterning. *Science* **375**, eaaw9021 (2022). doi: 10.1126/science.aaw9021; pmid: 34990240
9. T. Cumming, R. Levayer, Toward a predictive understanding of epithelial cell death. *Semin. Cell Dev. Biol.* **156**, 44–57 (2024). doi: 10.1016/j.semcdb.2023.06.008; pmid: 37400292
10. X. Ai, D. Wang, J. Zhang, J. Shen, Hippo signaling promotes Ets21c-dependent apical cell extrusion in the *Drosophila* wing disc. *Development* **147**, dev.190124 (2020). doi: 10.1242/dev.190124; pmid: 33028612
11. Y. Gu, T. Forostyan, R. Sabbadini, J. Rosenblatt, Epithelial cell extrusion requires the sphingosine-1-phosphate receptor 2 pathway. *J. Cell Biol.* **193**, 667–676 (2011). doi: 10.1083/jcb.201010075; pmid: 21555463
12. K. Duszyc *et al.*, Mechanotransduction activates RhoA in the neighbors of apoptotic epithelial cells to engage apical extrusion. *Curr. Biol.* **31**, 1326–1336.e5 (2021). doi: 10.1016/j.cub.2021.01.003; pmid: 33581074
13. D. M. Pritchard, C. S. Potten, S. J. Korsmeyer, S. Roberts, J. A. Hickman, Damage-induced apoptosis in intestinal epithelia from bcl-2-null and bax-null mice: Investigations of the mechanistic determinants of epithelial apoptosis in vivo. *Oncogene* **18**, 7287–7293 (1999). doi: 10.1038/sj.onc.1203150; pmid: 10602483
14. D. M. Pritchard *et al.*, Bcl-w is an important determinant of damage-induced apoptosis in epithelia of small and large intestine. *Oncogene* **19**, 3955–3959 (2000). doi: 10.1038/sj.onc.1203729; pmid: 10951589
15. C. Günther *et al.*, Caspase-8 regulates TNF-α-induced epithelial necroptosis and terminal ileitis. *Nature* **477**, 335–339 (2011). doi: 10.1038/nature10400; pmid: 21921917
16. F. Ghazavi *et al.*, Executioner caspases 3 and 7 are dispensable for intestinal epithelium turnover and homeostasis at steady state. *Proc. Natl. Acad. Sci. U.S.A.* **119**, e2024508119 (2022). doi: 10.1073/pnas.2024508119; pmid: 35105800
17. G. T. Eisenhoffer *et al.*, Crowding induces live cell extrusion to maintain homeostatic cell numbers in epithelia. *Nature* **484**, 546–549 (2012). doi: 10.1038/nature10999; pmid: 22504183
18. E. Marinari *et al.*, Live-cell delamination counterbalances epithelial growth to limit tissue overcrowding. *Nature* **484**, 542–545 (2012). doi: 10.1038/nature10984; pmid: 22504180
19. R. Levayer, C. Dupont, E. Moreno, Tissue Crowding Induces Caspase-Dependent Competition for Space. *Curr. Biol.* **26**, 670–677 (2016). doi: 10.1016/j.cub.2015.12.072; pmid: 26898471
20. C. Pérez-González, G. Ceada, M. Matejčić, X. Trepat, Digesting the mechanobiology of the intestinal epithelium. *Curr. Opin. Genet. Dev.* **72**, 82–90 (2022). doi: 10.1016/j.gde.2021.10.005; pmid: 34902705
21. R. M. Houtekamer, M. C. van der Net, M. M. Maurice, M. Gloerich, Mechanical forces directing intestinal form and function. *Curr. Biol.* **32**, R791–R805 (2022). doi: 10.1016/j.cub.2022.05.041; pmid: 35882203
22. T. F. Bullen *et al.*, Characterization of epithelial cell shedding from human small intestine. *Lab. Invest.* **86**, 1052–1063 (2006). doi: 10.1038/labinvest.3700464; pmid: 16909128
23. J. M. Williams *et al.*, A mouse model of pathological small intestinal epithelial cell apoptosis and shedding induced by systemic administration of lipopolysaccharide. *Dis. Model. Mech.* **6**, 1388–1399 (2013). doi: 10.1242/dmm.013284; pmid: 24046352
24. Y. Atieh, T. Wyatt, A. M. Zaske, G. T. Eisenhoffer, Pulsatile contractions promote apoptotic cell extrusion in epithelial tissues. *Curr. Biol.* **31**, 1129–1140.e4 (2021). doi: 10.1016/j.cub.2020.12.005; pmid: 33400921
25. T. Zulueta-Coarasa, J. Rosenblatt, The role of tissue maturity and mechanical state in controlling cell extrusion. *Curr. Opin. Genet. Dev.* **72**, 1–7 (2022). doi: 10.1016/j.gde.2021.09.003; pmid: 34560388
26. S. Curran *et al.*, Myosin II Controls Junction Fluctuations to Guide Epithelial Tissue Ordering. *Dev. Cell* **43**, 480–492.e6 (2017). doi: 10.1016/j.devcel.2017.09.018; pmid: 29107560
27. M. Michel, C. Dahmann, Tissue mechanical properties modulate cell extrusion in the *Drosophila* abdominal epidermis. *Development* **147**, dev179606 (2020). doi: 10.1242/dev.179606; pmid: 32161061
28. J. L. Teo *et al.*, Caveolae Control Contractile Tension for Epithelia to Eliminate Tumor Cells. *Dev. Cell* **54**, 75–91.e7 (2020). doi: 10.1016/j.devcel.2020.05.002; pmid: 32485139
29. R. N. U. Kok *et al.*, OrganoidTracker: Efficient cell tracking using machine learning and manual error correction. *PLOS ONE* **15**, e0240802 (2020). doi: 10.1371/journal.pone.0240802; pmid: 33091031
30. G. Huelsz-Prince *et al.*, Mother cells control daughter cell proliferation in intestinal organoids to minimize proliferation fluctuations. *eLife* **11**, e80682 (2022). doi: 10.7554/eLife.80682; pmid: 36445322
31. M. S. Levine, A. J. Holland, The impact of mitotic errors on cell proliferation and tumorigenesis. *Genes Dev.* **32**, 620–638 (2018). doi: 10.1101/gad.314351.118; pmid: 29802124
32. I. Bonnet *et al.*, Mechanical state, material properties and continuous description of an epithelial tissue. *J. R. Soc. Interface* **9**, 2614–2623 (2012). doi: 10.1098/rsif.2012.0263; pmid: 22628216
33. Q. Yang *et al.*, Cell fate coordinates mechano-osmotic forces in intestinal crypt formation. *Nat. Cell Biol.* **23**, 733–744 (2021). doi: 10.1038/s41556-021-00700-2; pmid: 34155381
34. C. Pérez-González *et al.*, Mechanical compartmentalization of the intestinal organoid enables crypt folding and collective cell migration. *Nat. Cell Biol.* **23**, 745–757 (2021). doi: 10.1038/s41556-021-00699-6; pmid: 34155382
35. A. Popkova *et al.*, A Cdc42-mediated supracellular network drives polarized forces and Drosophila egg chamber extension. *Nat. Commun.* **11**, 1921 (2020). doi: 10.1038/s41467-020-15593-2; pmid: 32317641
36. M. Behrndt *et al.*, Forces driving epithelial spreading in zebrafish gastrulation. *Science* **338**, 257–260 (2012). doi: 10.1126/science.1224143; pmid: 23066079
37. A. C. Martin, M. Kaschube, E. F. Wieschaus, Pulsed contractions of an actin-myosin network drive apical constriction. *Nature* **457**, 495–499 (2009). doi: 10.1038/nature07522; pmid: 19029882
38. A. Sutherland, A. Lesko, Pulsed actomyosin contractions in morphogenesis. *F1000 Res.* **9**, 142 (2020). doi: 10.12688/f1000research.20874.1; pmid: 32148766
39. Y. An *et al.*, Apical constriction is driven by a pulsatile apical myosin network in delaminating *Drosophila* neuroblasts. *Development* **144**, 2153–2164 (2017). doi: 10.1242/dev.150763; pmid: 28506995
40. S. Chanet *et al.*, Actomyosin meshwork mechanosensing enables tissue shape to orient cell force. *Nat. Commun.* **8**, 15014 (2017). doi: 10.1038/ncomms15014; pmid: 28504247
41. L. Valon, A. Marín-Llauradó, T. Wyatt, G. Charras, X. Trepat, Optogenetic control of cellular forces and mechanotransduction. *Nat. Commun.* **8**, 14396 (2017). doi: 10.1038/ncomms14396; pmid: 28186127
42. T. Matsushita *et al.*, Targeted disruption of mouse ortholog of the human MYH9 responsible for macrothrombocytopenia with different organ involvement: Hematological, nephrological, and otological studies of heterozygous KO mice. *Biochem. Biophys. Res. Commun.* **325**, 1163–1171 (2004). doi: 10.1016/j.bbrc.2004.10.147; pmid: 15555549
43. Y. Zhang *et al.*, Mouse models of MYH9-related disease: Mutations in nonmuscle myosin II-A. *Blood* **119**, 238–250 (2012). doi: 10.1182/blood-2011-06-358853; pmid: 21908426
44. M. F. Schliffka *et al.*, Multiscale analysis of single and double maternal-zygotic *Myh9* and *Myh10* mutants during mouse preimplantation development. *eLife* **10**, e68536 (2021). doi: 10.7554/eLife.68536; pmid: 33871354
45. J.-L. Maître *et al.*, Asymmetric division of contractile domains couples cell positioning and fate specification. *Nature* **536**, 344–348 (2016). doi: 10.1038/nature18958; pmid: 27487217
46. M. Rauzi, P. Verant, T. Lecuit, P.-F. Lenne, Nature and anisotropy of cortical forces orienting Drosophila tissue morphogenesis. *Nat. Cell Biol.* **10**, 1401–1410 (2008). doi: 10.1038/ncb1798; pmid: 18978783
47. M. Sivagnanam *et al.*, Identification of EpCAM as the gene for congenital tufting enteropathy. *Gastroenterology* **135**, 429–437 (2008). doi: 10.1053/j.gastro.2008.05.036; pmid: 18572020
48. J. L. Mueller, M. D. McGeough, C. A. Peña, M. Sivagnanam, Functional consequences of *EpCam* mutation in mice and men. *Am. J. Physiol. Gastrointest. Liver Physiol.* **306**, G278–G288 (2014). doi: 10.1152/ajpgi.00286.2013; pmid: 24337010
49. N. Maghzal, H. A. Kayali, N. Rohani, A. V. Kajava, F. Fagotto, EpCAM controls actomyosin contractility and cell adhesion by direct inhibition of PKC. *Dev. Cell* **27**, 263–277 (2013). doi: 10.1016/j.devcel.2013.10.003; pmid: 24183651
50. T. Ouchi, S. Morimura, L. E. Dow, H. Miyoshi, M. C. Udey, EpCAM (CD326) Regulates Intestinal Epithelial Integrity and Stem Cells via Rho-Associated Kinase. *Cells* **10**, 256 (2021). doi: 10.3390/cells10020256; pmid: 33525555
51. B. Das, M. Sivagnanam, Congenital Tufting Enteropathy: Biology, Pathogenesis and Mechanisms. *J. Clin. Med.* **10**, 19 (2020). doi: 10.3390/jcm10010019; pmid: 33374714
52. B. Das *et al.*, Aberrant Epithelial Differentiation Contributes to Pathogenesis in a Murine Model of Congenital Tufting Enteropathy. *Cell. Mol. Gastroenterol. Hepatol.* **12**, 1353–1371 (2021). doi: 10.1016/j.jcmgh.2021.06.015; pmid: 34198013
53. B. Das *et al.*, Enteroids expressing a disease-associated mutant of EpCAM are a model for congenital tufting enteropathy. *Am. J. Physiol. Gastrointest. Liver Physiol.* **317**, G580–G591 (2019). doi: 10.1152/ajpgi.00098.2019; pmid: 31433211

54. F. Meng *et al.*, Mechanical stretching boosts expansion and regeneration of intestinal organoids through fueling stem cell self-renewal. *Cell Regen.)* **11**, 39 (2022). doi: 10.1186/s13619-022-00137-4; pmid: 36319799
55. M. B. Baghdadi *et al.*, PIEZO-dependent mechanosensing is essential for intestinal stem cell fate decision and maintenance. *Science* **386**, eadj7615 (2024). doi: 10.1126/science.adj7615; pmid: 39607940
56. S. A. Gudipaty *et al.*, Mechanical stretch triggers rapid epithelial cell division through Piezo1. *Nature* **543**, 118–121 (2017). doi: 10.1038/nature21407; pmid: 28199303
57. M. E. Fernández-Sánchez *et al.*, Mechanical induction of the tumorigenic β-catenin pathway by tumour growth pressure. *Nature* **523**, 92–95 (2015). doi: 10.1038/nature14329; pmid: 25970250
58. A. U. Spencer *et al.*, Enterogenesis in a clinically feasible model of mechanical small-bowel lengthening. *Surgery* **140**, 212–220 (2006). doi: 10.1016/j.surg.2006.03.005; pmid: 16904972
59. H. A. Messal *et al.*, Tissue curvature and apicobasal mechanical tension imbalance instruct cancer morphogenesis. *Nature* **566**, 126–130 (2019). doi: 10.1038/s41586-019-0891-2; pmid: 30700911
60. L. Sui *et al.*, Differential lateral and basal tension drive folding of Drosophila wing discs through two distinct mechanisms. *Nat. Commun.* **9**, 4620 (2018). doi: 10.1038/s41467-018-06497-3; pmid: 30397306
61. R. Priya *et al.*, Tension heterogeneity directs form and fate to pattern the myocardial wall. *Nature* **588**, 130–134 (2020). doi: 10.1038/s41586-020-2946-9; pmid: 33208950
62. N. G. Naydenov *et al.*, Nonmuscle Myosin IIA Regulates Intestinal Epithelial Barrier in vivo and Plays a Protective Role During Experimental Colitis. *Sci. Rep.* **6**, 24161 (2016). doi: 10.1038/srep24161; pmid: 27063635
63. L. D. C. Martínez-Sánchez *et al.*, Epithelial RAC1-dependent cytoskeleton dynamics controls cell mechanics, cell shedding and barrier integrity in intestinal inflammation. *Gut* **72**, 275–294 (2023). doi: 10.1136/gutjnl-2021-325520; pmid: 35241625
64. A. A. van Bodegraven *et al.*, Genetic variation in myosin IXB is associated with ulcerative colitis. *Gastroenterology* **131**, 1768–1774 (2006). doi: 10.1053/j.gastro.2006.09.011; pmid: 17087940
65. H. Baribault, J. Penner, R. V. Iozzo, M. Wilson-Heiner, Colorectal hyperplasia and inflammation in keratin 8-deficient FVB/N mice. *Genes Dev.* **8**, 2964–2973 (1994). doi: 10.1101/gad.8.24.2964; pmid: 7528156
66. Y. Ma *et al.*, ACF7 regulates inflammatory colitis and intestinal wound response by orchestrating tight junction dynamics. *Nat. Commun.* **8**, 15375 (2017). doi: 10.1038/ncomms15375; pmid: 28541346
67. G. M. Slattum, J. Rosenblatt, Tumour cell invasion: An emerging role for basal epithelial cell extrusion. *Nat. Rev. Cancer* **14**, 495–501 (2014). doi: 10.1038/nrc3767; pmid: 24943812
68. T. W. Marshall, I. E. Lloyd, J. M. Delalande, I. Näthke, J. Rosenblatt, The tumor suppressor adenomatous polyposis coli controls the direction in which a cell extrudes from an epithelium. *Mol. Biol. Cell* **22**, 3962–3970 (2011). doi: 10.1091/mbc.e11-05-0469; pmid: 21900494
69. U. A. Hänninen *et al.*, Exome-wide somatic mutation characterization of small bowel adenocarcinoma. *PLOS Genet.* **14**, e1007200 (2018). doi: 10.1371/journal.pgen.1007200; pmid: 29522538
70. A. Nyga, S. Ganguli, H. K. Matthews, B. Baum, The role of RAS oncogenes in controlling epithelial mechanics. *Trends Cell Biol.* **33**, 60–69 (2023). doi: 10.1016/j.tcb.2022.09.002; pmid: 36175301
71. D. S. Bryan *et al.*, 4-Hydroxyacetophenone modulates the actomyosin cytoskeleton to reduce metastasis. *Proc. Natl. Acad. Sci. U.S.A.* **117**, 22423–22429 (2020). doi: 10.1073/pnas.2014639117; pmid: 32848073
72. P. Muenzner, M. Rohde, S. Kneitz, C. R. Hauck, CEACAM engagement by human pathogens enhances cell adhesion and counteracts bacteria-induced detachment of epithelial cells. *J. Cell Biol.* **170**, 825–836 (2005). doi: 10.1083/jcb.200412151; pmid: 16115956
73. M. Kim *et al.*, Bacteria hijack integrin-linked kinase to stabilize focal adhesions and block cell detachment. *Nature* **459**, 578–582 (2009). doi: 10.1038/nature07952; pmid: 19489119
74. A. C. Fasciano *et al.*, Yersinia pseudotuberculosis YopE prevents uptake by M cells and instigates M cell extrusion in human ileal enteroid-derived monolayers. *Gut Microbes* **13**, 1988390 (2021). doi: 10.1080/19490976.2021.1988390; pmid: 34793276
75. C. Pleguezuelos-Manzano *et al.*, Establishment and Culture of Human Intestinal Organoids Derived from Adult Stem Cells. *Curr. Protoc. Immunol.* **130**, e106 (2020). doi: 10.1002/cpim.106; pmid: 32940424
76. E. Izquierdo, T. Quinkler, S. De Renzis, Guided morphogenesis through optogenetic activation of Rho signalling during early Drosophila embryogenesis. *Nat. Commun.* **9**, 2366 (2018). doi: 10.1038/s41467-018-04754-z; pmid: 29915285
77. J. Beumer *et al.*, High-Resolution mRNA and Secretome Atlas of Human Enteroendocrine Cells. *Cell* **181**, 1291–1306.e19 (2020). doi: 10.1016/j.cell.2020.04.036; pmid: 32407674
78. J. L. Schmid-Burgk, K. Höning, T. S. Ebert, V. Hornung, CRISPaint allows modular base-specific gene tagging using a ligase-4-dependent mechanism. *Nat. Commun.* **7**, 12338 (2016). doi: 10.1038/ncomms12338; pmid: 27465542
79. B. Artegiani *et al.*, Fast and efficient generation of knock-in human organoids using homology-independent CRISPR-Cas9 precision genome editing. *Nat. Cell Biol.* **22**, 321–331 (2020). doi: 10.1038/s41556-020-0472-5; pmid: 32123335
80. M. Fujii, M. Matano, K. Nanki, T. Sato, Efficient genetic engineering of human intestinal organoids using electroporation. *Nat. Protoc.* **10**, 1474–1485 (2015). doi: 10.1038/nprot.2015.088; pmid: 26334867
81. X. Zheng *et al.*, Organoid cell fate dynamics in space and time. *Sci. Adv.* **9**, eadd6480 (2023). doi: 10.1126/sciadv.add6480; pmid: 37595032
82. J. Schindelin *et al.*, Fiji: An open-source platform for biological-image analysis. *Nat. Methods* **9**, 676–682 (2012). doi: 10.1038/nmeth.2019; pmid: 22743772
83. C. T. Rueden *et al.*, ImageJ2: ImageJ for the next generation of scientific image data. *BMC Bioinformatics* **18**, 529 (2017). doi: 10.1186/s12859-017-1934-z; pmid: 29187165
84. S. Herbert *et al.*, LocalZProjector and DeProj: A toolbox for local 2D projection and accurate morphometrics of large 3D microscopy images. *BMC Biol.* **19**, 136 (2021). doi: 10.1186/s12915-021-01037-w; pmid: 34215263
85. P. Virtanen *et al.*, SciPy 1.0: Fundamental algorithms for scientific computing in Python. *Nat. Methods* **17**, 261–272 (2020). doi: 10.1038/s41592-019-0686-2; pmid: 32015543

ACKNOWLEDGMENTS

We thank M. Kamp for assistance and maintenance of the imaging setups at AMOLF; Y. Goos for lab management; and G. Huelsz-Prince, X. Zheng, M. Betjes, P. Ender, M. Vennettilli, P. Rein ten Wolde, and all members of the Tans, van Zon, and Clevers laboratories for helpful discussion. We thank K. Sonnen and S. Wetering for kindly sharing equipment, technical support, and helpful discussions. We thank A. de Graaf and the Hubrecht imaging center for the maintenance of equipment. **Funding:** This work was supported by the Dutch Research Council, NWO Building Blocks of Life grant, no. 737.016.009 (R.N.U.K., J.V.Z., S.J.T.); the Dutch Research Council, NWO Groot grant, no. 2019.085 (W.K.S., J.V.Z., S.J.T., H.C.); the Netherlands Organization for Scientific Research, Gravitation Program “Materials Driven Regeneration,” no. 024.003.013 (D.K., J.V.E., H.C.); and the European Commission, H2020-MSCA-IF-2020, MCExtrusion no. 101026478 (D.K.). Funding was partially provided by Ecole Polytechnique Fédérale de Lausanne (EPFL) (M.N., N.G., M.L.). **Author contributions:** Conceptualization: D.K., W.K.S., J.V.E., J.V.Z., S.J.T., H.C.; Funding acquisition: D.K., J.V.E., J.V.Z., S.J.T., H.C.; Investigation: D.K., W.K.S., R.N.U.K., D.J.M., S.W., M.B.-H.; Methodology: D.K., W.K.S., M.N., N.G., M.L., J.V.E., D.J.M., S.W.; Project administration: D.K., W.K.S., J.V.E., J.V.Z., S.J.T., H.C.; Software: R.N.U.K., J.V.Z., W.K.S.; Supervision: J.V.E., J.V.Z., S.J.T., H.C.; Visualization: D.K., W.K.S., R.N.U.K.; Writing – original draft: D.K., W.K.S.; Writing – review & editing: D.K., W.K.S., J.V.Z., S.J.T., H.C. **Competing interests:** H.C. is head of Pharma Research and Early Development (pRED) at Roche. H.C. is inventor of several patents related to organoid technology; his full disclosure is given at https://www.uu.nl/staff/JCClevers/AncillaryActivities. M.N., M.B.-H., N.G., and M.L. are employees of Hoffmann-La Roche. M.N., M.L., and N.G. are named as inventors on patents (EP3541925A1, EP16199677.2, PCT/EP2017/079651, US20190367872A1, and CN110249044A) related to the scaffold-guided organoid technology used in this study; N.G. is additionally named as an inventor on patent WO2018091677A1. **Data and materials availability:** All data are available in the manuscript or the supplementary materials. Plasmids are available at Addgene.

SUPPLEMENTARY MATERIALS

science.org/doi/10.1126/science.adr8753
Figs. S1 to S9; Tables S1 and S2; Movies S1 to S11; MDAR Reproducibility Checklist

Submitted 19 July 2024; resubmitted 16 April 2025; accepted 12 June 2025

10.1126/science.adr8753